https://doi.org/10.5194/egusphere-2025-5179
Preprint. Discussion started: 19 February 2026

Mobile Zenith DOAS Measurements of NO_2 and HCHO, and their Relationship to Collocated In Situ measurements

Davis Earley[1], Elena Lind[1,3], James Flynn[2], Subin Yoon[2], Sergio Alvarez[2], and Travis Griggs[2]
[1]Virginia Polytechnic institute and State University: Blacksburg, Virginia, United States
[2]University of Houston: Houston, Texas, United States
[3]Goddard Space Flight Center: Greenbelt, Maryland, United States
Correspondence: Davis Earley (jeffreyde@vt.edu)

Abstract. The TRACER-AQ (TRacking Aerosol Convection interactions ExpeRiment- Air Quality) field campaign, performed in Houston, Texas in the summer of 2021, presented opportunities to compare Mobile DOAS (Differential Optical Absorption Spectroscopy) and in situ measurements of nitrogen dioxide (NO_2) and formaldehyde (HCHO), which can be used to obtain additional information about the vertical distribution of trace gas, without the need of a full sky scan.

During TRACER-AQ, a Zenith DOAS instrument retrieved Tropospheric Vertical Columns of NO_2, with typical columns ranging from 1–3$\times10^{16}$ $molecules\ cm^{-2}$ as well as HCHO columns, which typically ranged from 2.5–3.5$\times10^{16}$ $molecules\ cm^{-2}$. The retrieved columns were then compared to in situ measurements made on the same mobile lab in order to develop a Column to Surface Ratio, which describes the vertical heterogeneity of the measured columns. The average NO_2 ratio ranged from 100 m to 3 km, and HCHO from 200 m to 5 km. In addition, the Column to Surface Ratio was used on two case days to determine the origin of a local ozone episodes observed by the mobile lab.

1 Introduction

Mobile DOAS (Differential Optical Absorption Spectroscopy) (Platt, 1994; Platt and Stutz, 2008) instruments play a crucial role in remote sensing. For instance, Mobile DOAS instruments are effective at measuring trace gas distributions over regions (Constantin et al., 2013), identifying specific pollution sources (Wagner et al., 2010), and measuring emission fluxes around point sources as well as larger areas of interest (Johansson et al., 2009). Due to the difficulty of tracking the sun while in operation, Mobile DOAS instruments generally measure using the MAX-DOAS (Multi Axis DOAS) viewing geometry(Ibrahim et al., 2010) while observing a single direction relative to the mobile platform the instrument is operating on, and Zenith (Wang et al., 2012; Rivera et al., 2010) viewing geometries. However, areas that can be covered by a single Mobile DOAS instrument at a high spatial and temporal resolution can also be covered, more completely but at lower spatial and temporal resolutions, by airborne instruments, which are commonly used to measure trace gas columns over individual cities or similarly sized areas(Merlaud et al., 2011; Spinei et al., 2014). In addition, satellite-based instruments can measure entire continents on hourly

https://doi.org/10.5194/egusphere-2025-5179
Preprint. Discussion started: 19 February 2026

time scales, as in the case of geostationary instruments like the Tropospheric Emissions: Monitoring of Pollution (TEMPO) (Zoogman et al., 2017), or the entire planet daily, as in the case of sun synchronous instruments like TROPOMI (Ialongo et al., 2020; Goldberg et al., 2021).

Different viewing geometries have been developed to measure total, tropospheric and stratospheric gas columns by making use of each geometry's difference in sensitivity to radiative transfer processes and trace gas amounts in different altitudes. For instance, direct sun measurements are sensitive to total column abundance (Herman et al., 2009; Verhoelst et al., 2021; Spinei et al., 2014). The MAX-DOAS viewing geometry (pointing at various elevation angles relative to the horizon) is most sensitive to gas absorption in the lowest 2–3 km (Hönninger et al., 2004; Frieß et al., 2019; Chan et al., 2020; Tirpitz et al., 2021) and is used for profile retrievals of trace gases at solar zenith angles smaller than 75°. With the zenith viewing geometry (ZSL-DOAS) the instrument is pointing straight up and is sensitive to the total column with significant increase in sensitivity to stratospheric gases at twilight (Tack et al., 2015; Chen et al., 2009).

Nitrogen oxides (NO_x = NO + NO_2) are two trace gases that are critical contributors to tropospheric ozone (O_3) chemistry. The primary anthropogenic sources of NO_x are combustion processes, which are dominated by vehicle and industrial emissions, especially from fossil fuel based power generators (Robinson and Robbins, 1970). At urban locations, these emissions are known to reach concentrations high enough to pose a negative impact on human health (Hesterberg et al., 2009) both through direct inhalation as well as the inhalation of secondary products of NO_2, such as O_3. The short lifetime of tropospheric NO_2 (Schaap et al., 2015) leads to NO_2 remaining concentrated around its major sources. For the case of on-road Mobile DOAS measurements, typical NO_2 measurements will be of vehicular NO_2 emissions, however they can also be influenced by industrial emissions when in close enough proximity.

Formaldehyde (HCHO) is a common Volatile Organic Compound (VOC) found in the troposphere which is carcinogenic, genotoxic, and can be found in both molecular and particulate forms (Toda et al., 2014). HCHO can be formed as an intermediate product of oxidation of other VOCs (Brewer et al., 1984; Guenther et al., 1995), making anthropogenic sources of secondary HCHO harder to identify. VOCs are one of the major contributors to the O_3 cycle, and VOC emissions can drive the oxidation capacity of the atmosphere. Since HCHO is an intermediate oxidation product of many types of VOC's the trace gas is often used as a proxy to estimate VOC emissions in an area (Palmer et al., 2003; Shim et al., 2005). HCHO is directly linked to the oxidation capacity of the atmosphere where increases in formaldehyde lead to increases in oxidation rates, influencing the production of tropospheric O_3.

Houston, Texas, is one of the largest and most polluted cities in the United States. Houston presents a unique location for Mobile DOAS applications, with a high traffic volume due to both daily commuters as well as shipping traffic into Houston and Port Arthur. The Houston-Galveston Area also boasts a large number of petrochemical refineries that refine oil extracted in Texas and surrounding states. These refineries are known to be both primary (emitted from flares,) and secondary (oxidation of propene, ethene, and other VOCs) sources of HCHO (Wert et al., 2003). Due to the high volume of oil refined in Houston, the Houston-Galveston Area also receives a large number of commercial marine vessels. This unique set of trace gas sources has been the interest of many previous field campaigns. Prior to the TRACER-AQ field campaign, field campaigns such as the Texas Air Quality Study 1 and 2 (TexAQS 1 and 2) and the Study of Houston Atmospheric Radical Precursors (SHARP)

(Olaguer et al., 2014) have been held in the area. These studies utilized in situ and remote sensing measuring techniques at stationary sites, as well as onboard mobile platforms such as ground vehicles, ships, and aircraft to quantify air quality on time scales ranging from a few months to a few years.

Previous studies have focused on the relationship between the vertical column density and trace gas concentrations measured at the surface (Lamsal et al., 2008, 2014; Thompson et al., 2019). This relationship has been used primarily to validate satellite-based DOAS measurements using in situ instrument networks (Celarier et al., 2008; Boersma et al., 2009; Kim et al., 2017), while other studies have focused on estimations of mixing layer height to evaluate the impact of local meteorology on vertical mixing (Chang et al., 2022; Adams et al., 2023). In addition, proximity to trace gas sources have been shown to significantly impact the relationship between vertical column and surface concentration (Flynn et al., 2014).

1.1 TRACER-AQ field campaign

The TRacking Aerosol Convection interactions ExpeRiment- Air Quality (TRACER-AQ) was held in the Houston-Galveston area from August through September 2021 (Judd et al.). This field campaign sought to evaluate how O_3 formation varies spatially and temporally, validate chemical transport modeling as well as satellite measurements in preparation for the launch of TEMPO, and investigate the intersection between air quality and socioeconomic factors.

During the intensive operations a number of instruments were operated concurrently. In the air, a Gulfstream-V aircraft carried two instruments: the GEOstationary Coastal and Air Pollution Events (GEO-CAPE) Airborne Spectrometer (GCAS) ultraviolet-visible-near infrared (UV-VIS-NIR) airborne spectrometer retrieved columns of NO_2 and HCHO below the aircraft, while the The High Spectral Resolution LIDAR (HSRL)-2 provided vertical profiles of aerosol characteristics below the aircraft. The aircraft flight plans generally covered the entirety of Houston, and took approximately 2 hours to complete, allowing for 3 repetitions per day. Ground measurements included NASA Tropospheric O_3 LIDAR Network (TOLNet) instruments, which are portable LIDAR instruments capable of retrieving O_3 profiles from the surface to a maximum altitude of 8 km. Stationary Pandora spectrometers were also set up at TOLNet locations to retrieve vertical columns of NO_2 and HCHO nominally once a minute with full sky scans and retrieved vertical trace gas profiles every 20-30 minutes. Finally, ozonesondes provided balloon based vertical profiles of pressure, temperature, humidity, O3, and wind. The university of Houston operated a ground based mobile lab was operated during the intensive measurement period(Miller et al., 2020). Various in situ instruments in the lab included NO_x, HCHO, O_3, SO_2, and surface temperature, pressure, humidity. Mounted on the top of the mobile lab were a Pandora spectrometer with a modified sensor head set up to take measurements in a Zenith measuring geometry, and a ceilometer that measures planetary boundary layer (PBL) height (see Table 1). Further information about the TRACER-AQ field campaign can be found in the works by Flynn et al. (2022); Li et al. (2023); Griggs et al. (2024).

Mobile DOAS and in situ measurements collected during the TRACER-AQ campaign can be used to estimate the "equal mixing" layer height of NO_2 and HCHO through comparisons of the two quantities, called the Column to Surface Ratio (CSR). Mobile DOAS measurements are usually taken to detail the spatial distribution of trace gas columns, and typically lack knowledge on the vertical distribution of trace gases. The addition of an in situ instrument to a zenith DOAS instrument on the same mobile platform allows for evaluation of vertical distribution within the atmosphere. The two measurement techniques

Table 1. Instrumentation deployed during TRACER-AQ September 2021 and used in this work. Ozonesondes were launched at La Porte Airport. AERONET supported the campaign with additional sites.

Instrument Name / platform	Instrument Type	Data Product
Pandora / mobile	Sun–sky–moon Spectrometer	NO_2 VCD, HCHO VCD
Vaisala CL-31 (910 ± 10 nm) / mobile	Ceilometer	PBL Height, Backscatter Profiles
AERONET CIMEL (6 instruments) / fixed	Sun–sky–moon Photometer	SSA, ASY, AOD
GmbH AL4021 / mobile	In Situ HCHO Analyzer	Surface Concentrations of HCHO
2-channel chemiluminescence NO/NO_x Analyzer	In Situ NO_2 Analyzer	Surface Concentrations of NO_2
ozonesonde / airborne	Balloon-bourne in situ and weather monitor	Vertical profiles of air T and P (O_2O_2)

are sensitive to different parts of the atmosphere, with zenith DOAS measurements being sensitive to the total column of trace gas, and in situ sampling only surface air. This comparison provides a rapid estimation of vertical distributions, which when paired with mobile measurements, can provide estimations of vertical heterogeneity. However, the CSR is not a true layer mixing height but an effective height that assumes the trace gas was equally distributed through the lower part of atmosphere. High CSRs higher concentrations of trace gas aloft in comparison to the surface level while low CSRs indicate the majority of trace gas is concentrated near the surface.

In addition to the on-road sources, other off-road sources, such as industrial sites, and secondary photo-chemical processes, contribute to the total column and in situ observations. Comparing planetary boundary layer layer heights from ceilometer backscatter data on the mobile platform and trace gas CSRs, provides an opportunity to estimate presence of the elevated layers and spatial heterogeneity.

Using the results from the Mobile DOAS measurements performed during TRACER-AQ, this paper intends to demonstrate application of the CSRs as a vertical heterogeneity indicator. Extensive air mass factor (AMF) sensitivity studies were conducted to better quantify trace gas column uncertainties derived from zenith DOAS measurements due to aerosol scattering, and unknown gas profile. Aerosol properties were obtained from multiple AERONET sites (Holben et al., 2001) within the Houston-Galveston area and on-board ceilometer

This paper is organized into four sections. Section two describes the data collection methodology for the in situ and Mobile DOAS data sets, with a further description of the DOAS analysis technique used to retrieve vertical column densities, and a description of the radiative transfer simulations used to estimate zenith AMFs as well as the sensitivity studies used to estimate AMF error due to unknown aerosol composition and gas profiles. Section three summarizes results from the TRACER-AQ field campaign as well as two case studies demonstrating the CSR both while the instruments were stationary and in motion and discusses further applications of the CSR. Finally, section four concludes this study.

https://doi.org/10.5194/egusphere-2025-5179
Preprint. Discussion started: 19 February 2026

2 Measurements and analysis

In order to perform comparisons of surface concentrations and vertical columns, in situ and Pandora remote sensing instruments were placed onboard a mobile laboratory during September 2021 as part of collaborative efforts made during the intensive measurement period of TRACER-AQ. In situ measurements were conducted by the University of Houston. Concentrations of HCHO were obtained onboard the mobile lab from an Aero-laser GmbH AL4021 HCHO Analyzer over 10 second measuring periods. Measurements of NO_2 were made using a custom 2-channel chemiluminescence NO/NO_x instrument with a UV-LED photolytic NO_2 converter, at a 1 second measurement interval but averaged to 10 seconds.

During the TRACER-AQ field campaign, one Pandora spectrometer was mounted on top of the mobile laboratory and fixed in the Zenith viewing direction. Pandora Instruments perform hyper-spectral measurements using an Avantes spectrometer, with a spectral resolution of 0.6 nm per FWHM and a wavelength range between 300 and 525 nm. The spectrometer and controlling computer are housed inside the mobile lab, while the sensor head, which has a field of view of $1.5°$, collects light outside the vehicle and is connected by a 400 μm core optical fiber cable. By pointing in the zenith direction, the instrument "sampled" the air masses directly overhead of the mobile lab. Raw spectra, corrected for instrumental effects, were used to determine differential slant column densities (ΔSCD), with a reference spectrum measured at the end of the Texas City dike in Galveston Bay. Next AMFs were simulated using the MYSTIC(Mayer, 2009) radiative transfer simulation software, using mean aerosol properties retrieved from a collection of six AERONET instruments within the Houston-Galveston area and vertical profiles from the ceilometer backscatter signal. These AMFs were used to estimate the residual trace gas column present in the reference spectrum, which is removed from the ΔSCD, as well as the stratospheric component of the NO_2 vertical column density for both NO_2 retrievals.

2.1 Pandora spectroscopic measurements: from spectra to trace gas ΔSCD to VCD

The DOAS technique is based on the modified Beer-Lambert law, which describes the spectral attenuation of electromagnetic radiation by molecular and aerosol absorption and scattering. As solar light propagates through the atmosphere, it interacts with atmospheric constituents and as a result, “carries their signatures.” The DOAS technique is capable of separating molecular absorption from molecular scattering and aerosol extinction due to the unique “differential” structure in the trace gas molecular absorption cross-sections (Platt and Stutz, 2008). Since molecular (Rayleigh) and aerosol (Mie) scattering show only smooth wavelength dependence, they can be easily estimated and removed by fitting a low order polynomial function (P_L). Equation 1 depicts the DOAS principle where the differential absorption by all the gases absorbing at the specified wavelength region is separated from the broadband extinction:

$$\ln \frac{I_o(\lambda,\mu^{ref})}{I(\lambda-\Delta\lambda,\mu)-offset(\lambda)} = \sum_{i=1}^{i=N} \Delta\tau(\lambda,T)_i + P_L = \sum_{i=1}^{i=N} \sigma(\lambda,T)_i \cdot \Delta SCD_i + P_L \tag{1}$$

Where, $I(\lambda)$ is the measured attenuated solar intensity at wavelength λ with potential wavelength shift $\Delta\lambda$ and observation geometry μ; $I_o(\lambda)$ is measured reference solar intensity at λ and observation geometry μ^{ref}; $\tau(\lambda,T)$ is the absorption optical depth caused by gas i absorption at λ and effective temperature T along the average photon path. DOAS fitting estimates differential slant column densities of each gas along the average photon path relative to the slant column density in the reference geometry ($\Delta SCD_i = SCD_i - SCD_i^{ref}$).

The raw spectra measured by the Pandora system are corrected for dark current, non-linearity, spectrometer latency, pixel response non-uniformity, and stray light according to standard Pandonia Global Network procedures (Cede, 2021). Pandora instrument calibration was done at Virginia Tech both before and after the TRACER-AQ field campaign. High resolution trace gas molecular absorption cross section spectra (see Table 2) were convolved with the wavelength dependent instrument slit function derived from the measures response to the atomic emission lines (Cede, 2021)

DOAS fitting of NO_2, HCHO, and the Oxygen Collisional Complex (O_2O_2) (from the corrected measurement and reference spectra) was done using the QDOAS (Version 3.4.5) software (Dankaert et al., 2017) at three different fitting windows: two for NO_2 (UV and VIS) and one for HCHO (UV). Table 2 lists corresponding fitting windows with their fitting parameters. In addition, a pseudo cross-section was generated to account for the Ring Effect (Grainger and Ring, 1962) using the QDOAS Ring tool following the method described by (Chance and Spurr, 1997). I_o correction was also performed for O_3 and NO_2 for all applicable fitting windows following the CINDI-2 protocols, using $I_o = 10^{20}$ and $I_o = 10^{17}$, respectively.

Table 2. DOAS fitting parameters used to retrieve HCHO, NO_2, and O_2O_2 ΔSCD from Pandora zenith sky measurements. The fitting windows are ordered starting with HCHO, NO_2 Ultraviolet, then NO_2 Visible retrievals.

Fitting Windows: HCHO (336.5–359 nm), NO_2 (UV: 338–370 nm), NO_2 (VIS: 425–490 nm)
Polynomial Order: 5
Offset and wavelength shift polynomial order: 1

Trace Gas	Temperature (K)	Source	Fitting Windows
NO_2	294, 220	Vandaele et al. (1998)	HCHO, NO_2 (UV, VIS)
H_2O	290	Rothman et al. (2013)	NO_2 (VIS)
O_3	243, 223	Serdyuchenko et al. (2014)	HCHO, NO_2 (UV, VIS)
O_2O_2	293	Thalman and Volkamer (2013)	HCHO, NO_2 (UV, VIS)
HCHO	297	Meller and Moortgat (2000)	HCHO, NO_2 (UV)
BrO	224	Fleischmann et al. (2004)	HCHO
Ring	270	Chance and Spurr (1997)	HCHO, NO_2 (UV, VIS)

Retrieval of NO_2 and O_2O_2 from UV and VIS fitting windows from zenith measurements are of interest from a radiative transfer point of view due to the difference in scattering height between them, especially at increasing solar zenith angles and the potential of using O_2O_2 for VCD calculations (Hönninger et al., 2004). SCD is an averaged over the photon path gas column and needs to be corrected by the AMF at the effective fitting window wavelength and scattering conditions (aerosols, Rayleigh), and observation geometry (pointing direction and solar zenith angle).

To derive the tropospheric column from the zenith measurements, first SCD_{ref} needs to be determined for NO_2, O_2O_2 and HCHO to calculate the total SCD. Considering that the stratospheric NO_2 abundance is non-negligible, it needs to be

https://doi.org/10.5194/egusphere-2025-5179
Preprint. Discussion started: 19 February 2026

subtracted from the total VCD for each measurement (Chen et al., 2009; Tack et al., 2015; Constantin et al., 2013). The relationship between slant path and vertical path is expressed as AMF.

$$VCD_{gas}^{trop}\left[molecules\ cm^{-2}\right] = VCD_{gas}^{total} - VCD_{gas}^{strat} = \frac{\Delta S_{gas}(\lambda,\mu) + S_{gas}^{ref}(\lambda,\mu^{ref})}{AMF(\lambda,\mu)} - VCD_{gas}^{strat} \tag{2}$$

The reference spectrum was created as an average of 1 hr of continuous measurements around local noon at the fixed location, the Texas City dike, on September 21, where the instruments operated between 10:00 and 13:00 CDT. Texas City is located directly south of the Houston Metropolitan Area, and has a large dike that extends 8 km from coast. Under south winds it is upwind from the local petrochemical industry, and can have relatively pollution free conditions. Figure A10 shows the driving route taken on September 21, with the dike located in the bottom right corner of the figure. As can be seen in Figure A10, while the location was largely free of NO_2, background HCHO levels at the dike were consistent with other measurements made along the coast of Galveston Bay.

2.2 Air Mass Factor calculations: sensitivity study

In most scattered sky DOAS applications, AMF determination must account for aerosol properties and vertical profiles, as well as for the trace gas profiles through radiative transfer simulations. Since this information is rarely available, previous Mobile DOAS studies deployed to estimate emission fluxes relied on the geometric approximation to estimate the AMF (Johansson et al., 2009; Wagner et al., 2010). Other mobile DOAS studies, such as Wang et al. (2012), Wu et al. (2017), and Pettinari et al. (2022) have evaluated effect of aerosol and gas profile information on AMF determination using radiative transfer models.

The AMF sensitivity studies in this work were designed to quantify how atmospheric structure and aerosol properties influence zenith-sky radiative transfer relevant to trace gas retrievals. The objective of these studies was to assess AMF dependence on aerosol optical depth, aerosol optical properties, aerosol vertical distribution, and boundary-layer dynamics under representative Houston conditions. Radiative transfer simulations spanning a range of solar zenith angles were conducted to identify key parameters controlling zenith-sky sensitivity. This study evaluates AMF of O_2O_2 ($\lambda_{eff} = 360$ and 477 nm), NO_2 ($\lambda_{eff} =$ 360 and 460 nm) and HCHO ($\lambda_{eff} = 340$ nm) at their corresponding effective wavelengths using:

1. AERONET aerosol properties (Holben et al., 2001), aerosol optical depth (AOD), single scattering albedo (SSA) and asymmetry parameter (ASY), in the greater Houston-Galveston Area area: Aldine, Liberty, Sugar Land, University of Houston Coastal Research Center, the University of Houston Main Campus, and Atmospheric Radiation Measurement site located at La Porte Regional Airport. AERONET is the standard of aerosol remote sensing and often is used to quantify aerosol properties and loadings in DOAS data interpretation.

2. aerosol vertical distribution estimation from the ceilometer backscatter signal (onboard the mobile lab). Ceilometer technology is another common data source for aerosol vertical distribution information.

3. eight vertical profiles estimating potential distribution of trace gases matching the profiles used in Frieß et al. (2019)

1D radiative transfer (RT) simulations were conducted using LibRadtran/MYSTIC package (Emde et al., 2016; Schwaerzel et al., 2020) to estimate measurement sensitivity as a function of hight (box AMF: bAMF). To obtain a total AMF at a specific observation geometry, trace gas bAMF (as a function of height) needs to be multiplied by the gas profile and integrated over the entire atmosphere. Trace gas $bAMF(\lambda,\mu)$ depends only on the aerosol scenario (aerosol type, vertical distribution and loading) and can be applied to NO_2, HCHO, and O_2O_2 only by varying the gas profile. The Henyey–Greenstein phase function is calculated from the estimated AERONET ASY as a simple analytic approximation of the true phase function. The surface albedo was assumed to be 0.15, representing the estimated albedo of both asphalt and concrete (Li et al., 2013), which the mobile lab can be expected to be driving on at any point in time.

2.2.1 Input data preparation into LibRadtran:

Aerosols properties: Daily aerosol SSA and ASY, representative of the entire Houston-Galveston area (mean $\pm 2\sigma$), were calculated from the AERONET inversion results from all considered sites. Note, that SSA and ASY have higher uncertainties at lower AODs (e.g. AOD < 0.4 at 440 nm) and this approach gives a more realistic view of the errors if AERONET is used to define aerosol type in RT simulations. Hourly AODs (for each day), were calculated from the AERONET direct sun measurements, which are shown in Figure 5 for 870 nm. SSA, ASY and AOD were interpolated / extrapolated to the corresponding wavelengths.

Aerosol extinction coefficient profiles at the effective wavelengths: Aerosol extinction profiles were calculated from the backscatter The ceilometer data and AERONET AOD measurements according to Wagner et al. (2019). Ceilometer backscatter

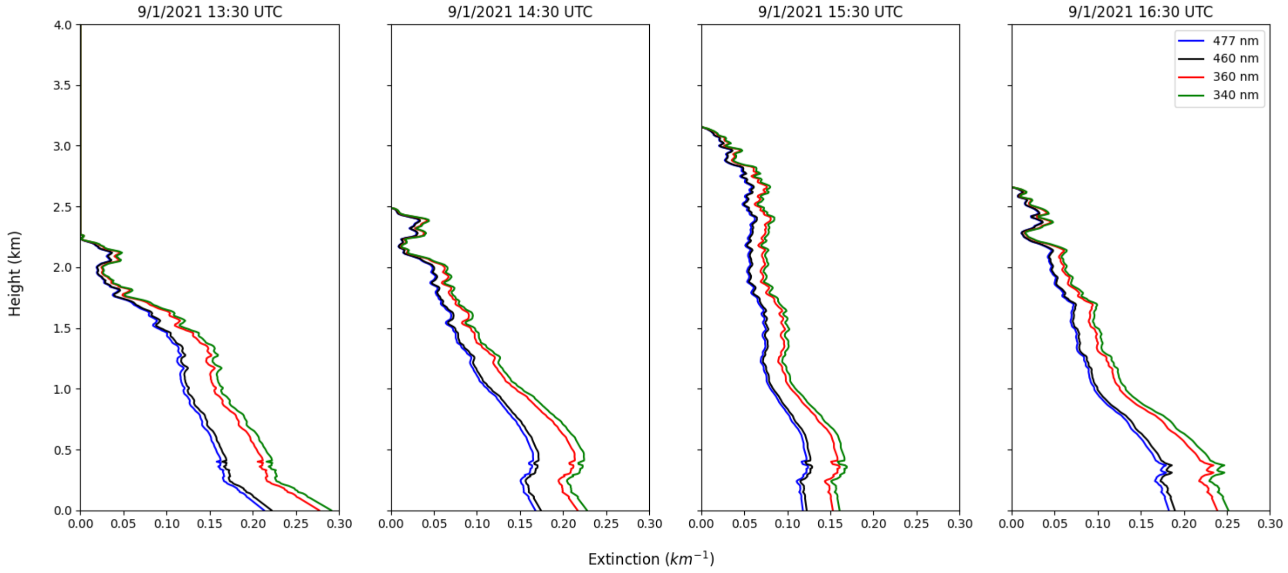

Figure 1. The aerosol extinction coefficient profiles derived from the 910 nm backscatter Ceilometer measurements and AERONET AOD , scaled to 477 nm (blue), 460 nm (red), 360 nm (red) and 340 nm (green).

https://doi.org/10.5194/egusphere-2025-5179
Preprint. Discussion started: 19 February 2026

signal at 910 nm first was averaged at an hourly rate, with further smoothing applied using a first order Savitzky–Golay filter on the backscatter profile above 500 m to account for increased noise at higher atmospheric levels. Resulting profiles were "zeroed" after the first negative value was encountered. Because the ceilometer had a minimum range of 100 m, the profile is linearly extrapolated below 100 m to the slope measured from 100 m to 200 m in order to obtain the full backscatter profile. Since the Ceilometer operated at 910 nm, the backscatter profiles must first be normalized by the AOD at 910 nm:

$$N = AOD_{910}/B_{int} \tag{3}$$

where AOD_{910} is the AOD value at 910 nm, B_{int} is the integrated backscatter profile up to 4 km. However, AERONET instruments do not measure AOD at 910 nm, and the AOD retrieved at 870 nm and 1020 must be used to calculate the Angstrom exponent

$$\alpha = -\frac{ln(\frac{AOD_{1020}}{AOD_{870}})}{ln(\frac{1020}{870})} \tag{4}$$

$$AOD_{910} = AOD_{870} \cdot \left(\frac{910nm}{870nm}\right)^{\alpha} \tag{5}$$

where α is the Angstrom exponent between 870 nm and 1020 nm, and AOD_{870} is the AOD at 870 nm. Next, the profiles are scaled to the AOD at the desired wavelength. Finally, the aerosol extinction coefficient profiles are interpolated onto the same altitude grid as the atmospheric profiles used for the simulations. Figure 1 shows the final extinction profiles scaled by the AOD at 477, 460, 360, and 340 nm. This process led to 280 unique aerosol scenarios, each with an aerosol profile for 477, 460, 360, and 340 nm, totaling 1368 profiles. Using this process, three sets of aerosol profiles were created, representing the statistical high, low, and mean aerosol profiles based on the AOD measured in the area.

Atmospheric temperature, pressure, relative humidity, O_3 and oxygen collision complex: Daily meteorological, O_2O_2 and O_3 profile inputs were generated from the ozonesonde data launched at La Porte Airport between 1–3 times each day. Information above the burst height was supplemented by the standard US atmosphere provided by the libRadTran profile library. O_2O_2 profiles were calculated from T, P, RH data at each altitude according to Spinei et al. (2014).

Trace gas profiles: To evaluate effect of trace gas tropospheric profiles on the $AMF(gas)$ seven trace gas profiles were selected from the MAX-DOAS inter-comparison study by Frieß et al. (2019), more information can be found in Figure 2 and Table 3.

These profiles were used to estimate AMFs under mean aerosol conditions. Stratospheric NO_2 profile dependence on time/SZA was not accounted for in these simulations.

Base case scenario: This scenario describes the aerosol property and trace gas inputs in case if these inputs were not varied.

The default aerosol conditions used as a baseline for this study are defined in (Shettle, 1990), which describe a rural type aerosol within the boundary layer, and background aerosol above 2 km with an estimated visibility of 50 km. The HCHO

Table 3. Description of trace gas tropospheric profiles evaluated in sensitivity study

Profile	Description	VCD ($\times 10^{15}$ $molecules\ cm^{-2}$)	Max Concentration($\times 10^{11}$ $molecules\ cm^{-3}$)
Profile 1	Exponential, 1 km Scale Height	5.00	0.48
Profile 2	Exponential, 1 km Scale Height	19.99	1.90
Profile 3	Exponential, 0.250 km Scale Height	9.93	3.27
Profile 4	Box Profile, 100 m Height	5.00	5.00
Profile 5	Box Profile, 200 m Height	5.00	2.50
Profile 6	Box Profile, 1 km Height	10.00	1.00
Profile 7	Gaussian at 1 km, 300 m FWHM	10.00	1.31

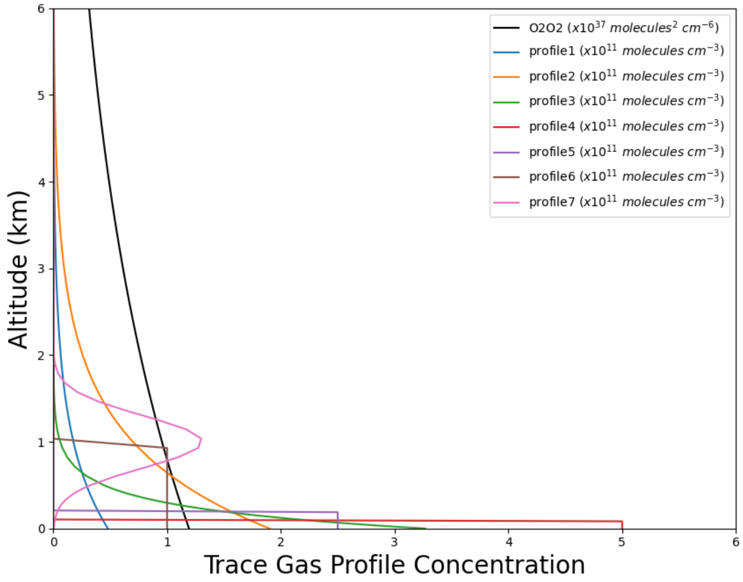

Figure 2. The vertical profiles used in the 2019 MAX-DOAS profile inter-comparison study(Frieß et al., 2019). These profiles serve as the basis for the profile-based portion of the sensitivity study. Details on the profile shape are provided in Table 3. In addition, the vertical profile of O_2O_2 (black) is included, which is derived from the mean atmospheric conditions measured by balloon sondes launched during TRACER-AQ.

profile was modeled as a box profile with a 1 km height and a concentration matching the mean concentration observed by the mobile HCHO in situ instrument. US standard atmosphere NO_2 profile was scaled at the surface with the mean concentration observed by the NO_2 in situ instrument.

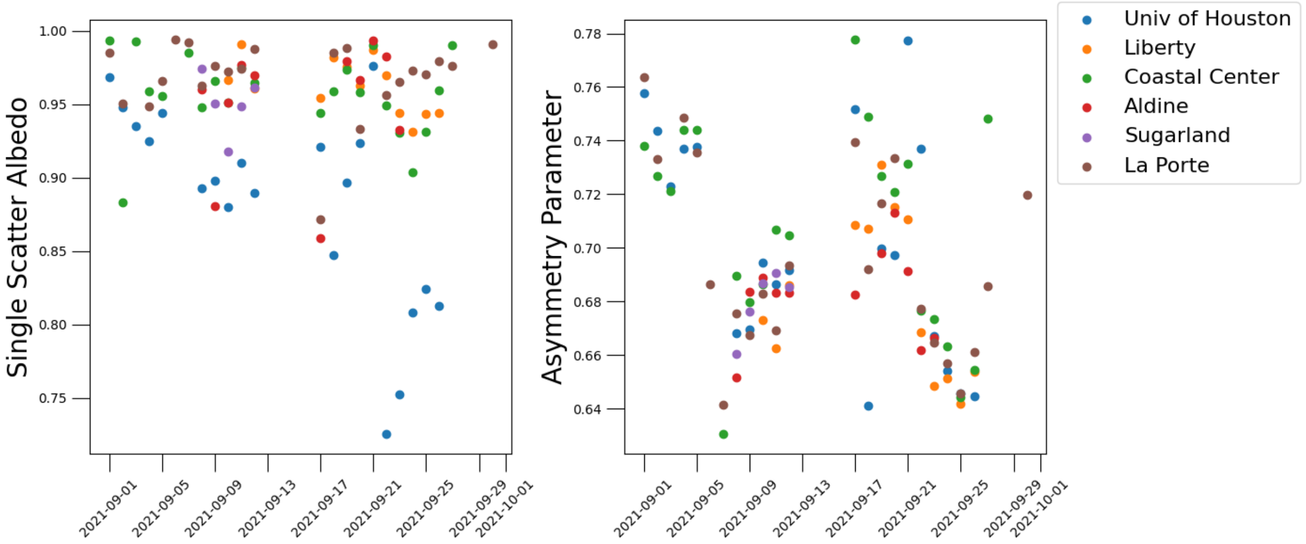

Figure 3. Daily mean values of L2 single scattering albedo(a) and asymmetry parameter(b) data, retrieved from six AERONET instruments at 440 nm in the Houston-Galveston-Brazoria area during September 2021.

2.3 Effect of Aerosol SSA and Asymmetry Parameter on AMF(O_2O_2)

Figure 3 shows the daily mean values of SSA and ASY for the six AERONET sited during TRACER-AQ. Typical values of the ASY range from 0.625 to 0.8 throughout September 2021, with daily differences in instruments ranging between 0.05 and 0.15. Apart from the AERONET site at the University of Houston, which is considered an urban location, the SSA retrieved are close to 1.0, with almost all retrieved SSA's being above 0.7. Typical differences in instrument retrievals, however range between 0.05 and 0.2, with the instrument located at the University of Houston largely determining the standard deviation of each day's dataset. The aerosol SSA and ASY were individually changed from their measured minimum to maximum in ten steps, and the model was run at each step at 477 nm and 360 nm for ten SZA's from 0° to 90°. The calculated box AMFs were then used to determine AMFs of O_2O_2, a trace gas with a consistent profile dependent on the vertical profile of air.

Figure 4 shows the shift in the AMFs for O_2O_2 as both SSA and ASY are increased from minimum values. At both UV and Visible wavelengths, SSA increasingly deviated from the minimum AMF, with solar zenith angles closer to the horizon seeing larger deviations than solar zenith angles closer to zenith. In spite of this, AMFs at both wavelengths only deviate at a maximum of 0.2 from the AMFs retrieved at the minimum SSA and ASY. At each solar zenith angle, the deviation is approximately linear, with increasing solar zenith angle increasing the rate of deviation. Because of this linear nature, and with a maximum daily deviation of the SSA of 0.2, the error due to an incorrect SSA estimate is closer to 2.5% for most solar zenith angles, and 5% for larger solar zenith angles, at both 477 nm and 360 nm.

The ASY, on the other hand, has an inverse linear relation to increasing values, and is much more sensitive to the retrieval wavelength than the SSA, with maximum differences in the AMF at 360 nm reaching up to 0.15. In addition, low solar zenith

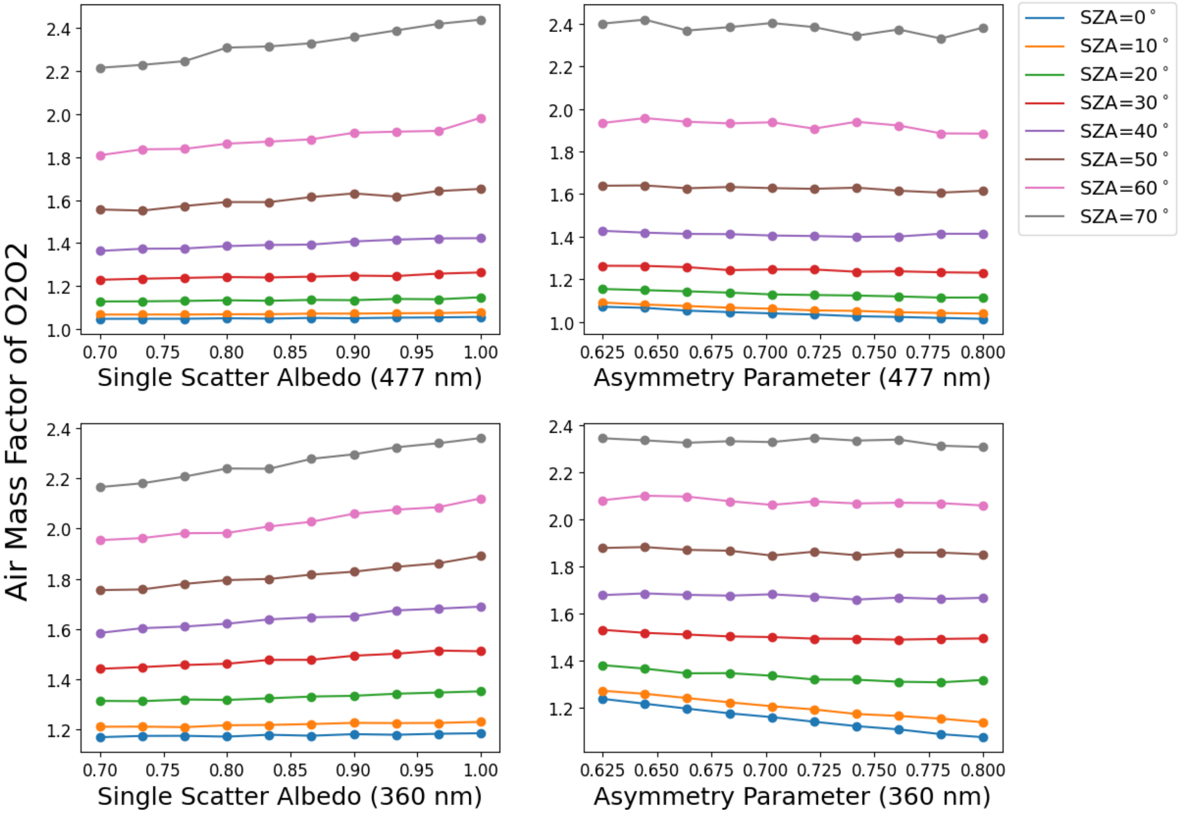

Figure 4. The AMF for O_2O_2 as the SSA was increased from 0.7 to 1.0, for 477 nm(a) and 360 nm(c), as well as AMFs for O_2O_2 as the asymmetry parameter was increased from 0.625 to 0.8 for 477 nm(b) and 360 nm(d). Each line corresponds to the solar zenith angle used to retrieve AMFS, from 0° to 70° in 10° increments.

angles, in particular 0° and 10°, show much larger deviations than larger solar zenith angles. However, the minimum solar zenith angle in Houston in September is close to 20° which show much lower deviations behaves much more similarly to the rest of the solar zenith angles tested. As such, the maximum deviation of the retrieved AMFs due to errors in the ASY estimation amount to 2.5% at 477 nm, and 5% at 360 nm. 265

2.4 Effect of aerosol loading and profile on AMF(O_2O_2)

The aerosol extinction coefficient profiles calculated above from the ceilometer and AERONET data were used to estimate AMFs for O_2O_2. Figure 6 shows the deviation of AMFs for O_2O_2 under high and low aerosol loadings compared to the mean aerosol conditions. Deviations from mean aerosol conditions are very consistent for most solar zenith angles, however at high solar zenith angles ($> 70°$), the error begins to compound, as the light begins to travel more and more through the upper parts 270 of atmosphere. AMF retrieval errors at 477 nm remain consistently less than ±0.05 outside of large solar zenith angles, and are

https://doi.org/10.5194/egusphere-2025-5179
Preprint. Discussion started: 19 February 2026

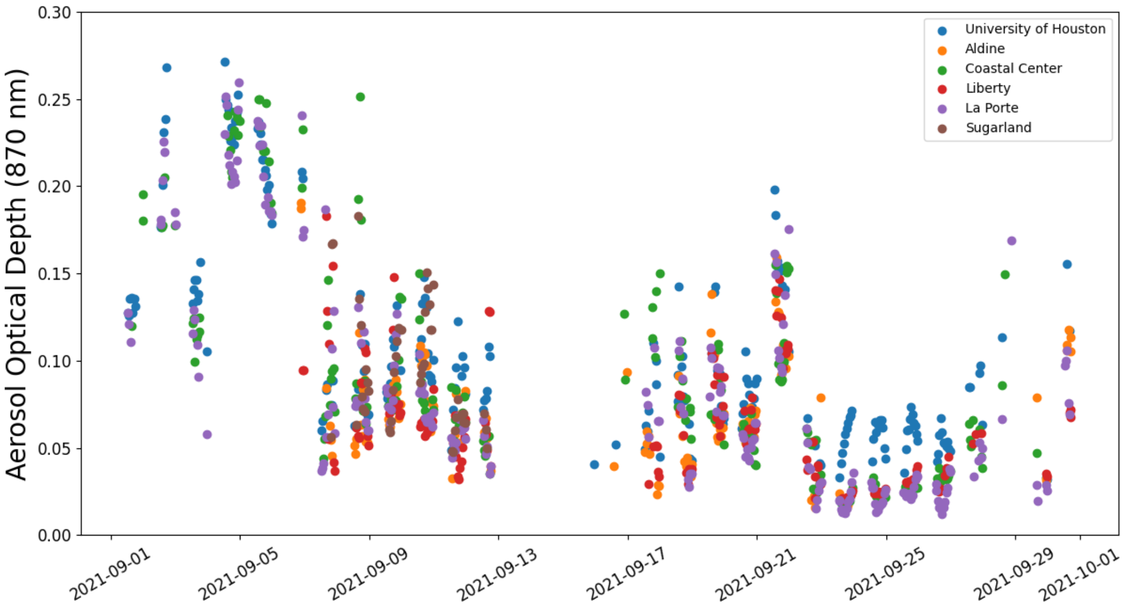

Figure 5. Time series of the L2 AOD values retrieved at 870 nm from six AERONET sites in the Houston-Galveston-Brazoria area during TRACER-AQ, averaged every one hour.

not sensitive to solar zenith angle. This behavior indicates that, outside of twilight, deviations of AMF are not sensitive to the solar zenith angle. The retrievals at 360 nm, however, are much more sensitive to the potential differences in aerosol conditions, with differences in both the high and mean conditions as well as the low and mean conditions being twice as large as their 275 visible counterparts, close to ± 0.1 outside of high solar zenith angles. For all of the aerosol scenarios tested, the standard deviation (2σ) was approximately 5% at 477 nm and 7.5% at 360 nm, which means that error due to incorrect aerosol profiles is expected to remain below 5% for visible AMFs and 7.5% for UV AMFs.

2.5 Effect of trace gas profile on AMF(gas)

Due to the mobile measurements of highly variable gases (e.g. NO_2), the zenith DOAS is expected to sample air with significant 280 difference in vertical distribution of trace gases. O_2O_2 absorption is widely used in DOAS community as a proxy for scattering processes due to its independence of emissions and sinks. In this study we also evaluate the differences between O_2O_2 and the selected trace gas AMF.

Figure 7 shows that at both 477 nm and 360 nm, the $AMF(O_2O_2)$ is larger than $AMF(gas)$. Diurnal differences are potentially attributed to higher O_2O_2 concentrations in free troposphere compared to NO_2 and HCHO. Outside of high solar 285 zenith angles, UV O_2O_2 AMFs remain 0.2–0.4 larger than the AMF retrieved from the other trace gas profiles, with a clear

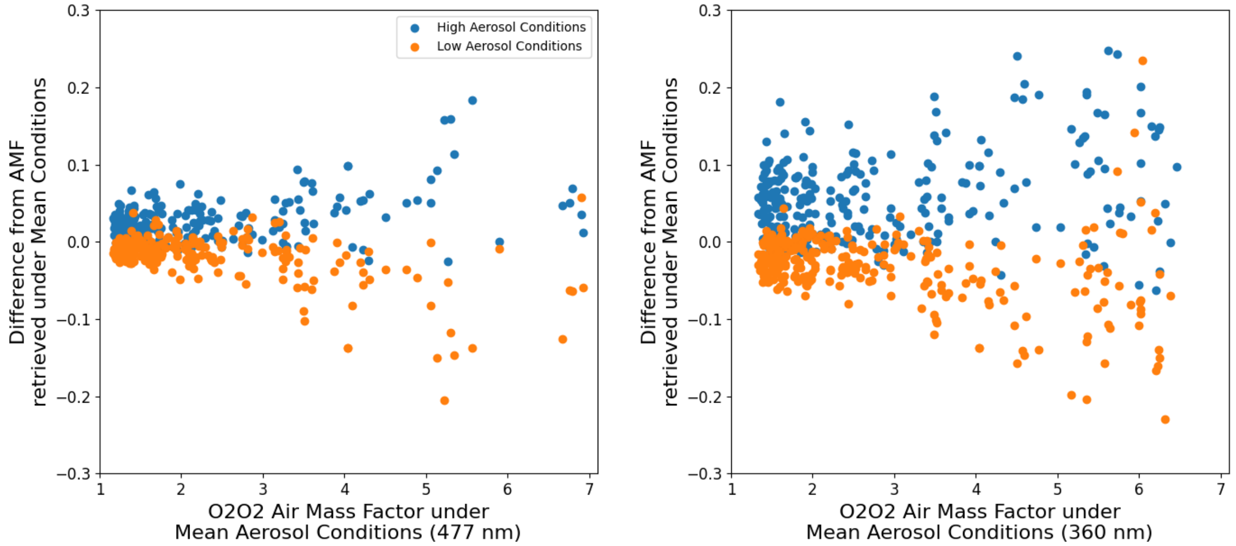

Figure 6. The absolute difference between O_2O_2 AMFs retrieved from high and mean aerosol conditions (blue) and from low and mean aerosol conditions (orange) plotted as a function of O_2O_2 AMF retrieved from mean aerosol conditions for 477 nm retrievals(a) and 360 nm retrievals(b).

solar zenith angle dependency. Visible AMF differences are much smaller, with O_2O_2 AMFs remaining between -0.08 and -0.2 outside of high solar zenith angles.

While these errors are large when compared to the effect of spatial averaging of the aerosol conditions, the differences between AMFs has a linear relation, as can be seen in Figure 8. For both UV and Visible wavelengths, the AMFs retrieved from the O_2O_2 profile and the other profiles are closely correlated ($r^2 > 0.97$) and have similar linear behaviors. As such, it is feasible to correct the O_2O_2 AMFs to agree with the AMFs retrieved from the profiles. Figures 7 c) and d) show the differences between the corrected O_2O_2 AMFs and AMFs retrieved from the profiles. After correction, the maximum difference is closer to ± 0.1 for UV and ± 0.05 for Visible wavelengths, with a clear solar zenith angle dependence. In addition, in individual profiles deviations are less than 5% from other profiles, which shows that the seven profiles chosen likely agree with each other better than with the O_2O_2 profile. This indicates that the changing of the vertical profile will impact the AMF by approximately 5%, which when combined with the assumptions made for the aerosol conditions, leads to a total estimated uncertainty of 15% for Visible AMF retrievals, and 20% for UV AMF retrievals.

Because both the O_2O_2 and NO_2 (profile 1 and 2) have similar profile shapes (exponential), both profiles produce similar AMF. This was demonstrated in Figure 8, where at both visible and UV wavelengths NO_2 and O_2O_2 AMFs were highly correlative, and only a slight correction factor was required to produce similar result. This comparison between AMFs, however, assumes a constant profile for both NO_2 and O_2O_2. The correction of the O_2O_2 AMFs to match the expected NO_2 AMFs is much lower than the expected error of the AMF, and as such is not significantly contributing to the AMF error.

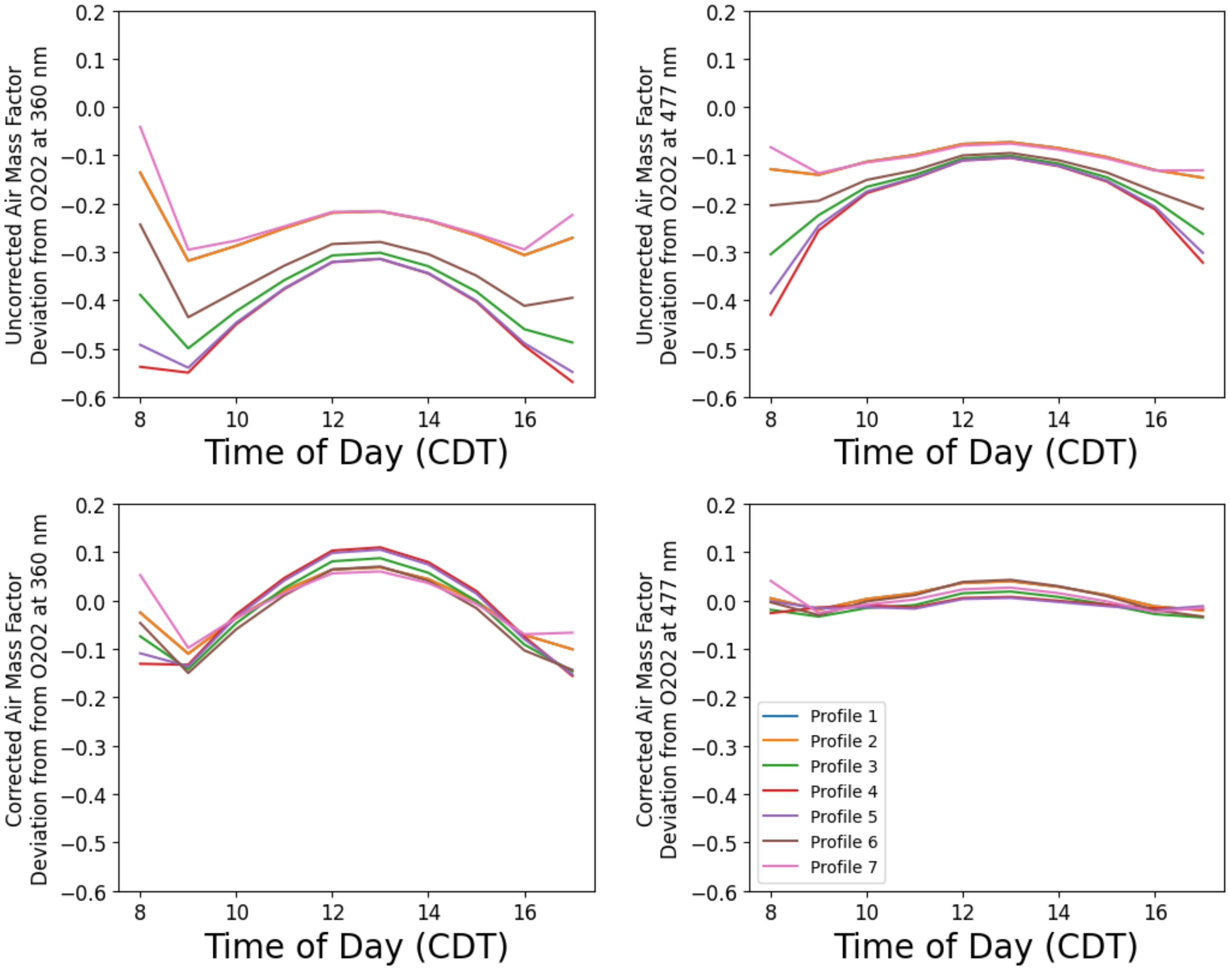

Figure 7. The diurnal average of uncorrected differences between the AMFs retrieved from the seven profiles and the O_2O_2 profile in the UV band (a) and Visible band (b), as well as the diurnal average of corrected differences between the AMFs retrieved from the seven profiles and the O_2O_2 profile at 360 nm(c) 477 nm(d).

Prior ZSL-DOAS works have assumed a single profile for NO_2 (Constantin et al., 2013; Wang et al., 2012) or utilized lookup tables based on prior measurement campaigns (Tack et al., 2015), however both methods require making assumptions about 305 the vertical profile of NO_2, which is not measurable through Mobile DOAS. In lieu of these assumptions, the O_2O_2 profile is much more easily estimable through the use of ozonesonde or surface measurements of pressure, temperature, and relative humidity, reducing the impact of profile mismatch. However, the error of the AMF largely originates from the wrong profile being used. While the AMFs can be linearly corrected, the true observed profile must be estimated in order to minimize the error, and is effectively the same as choosing a more accurate a priori profile to generate AMFs.

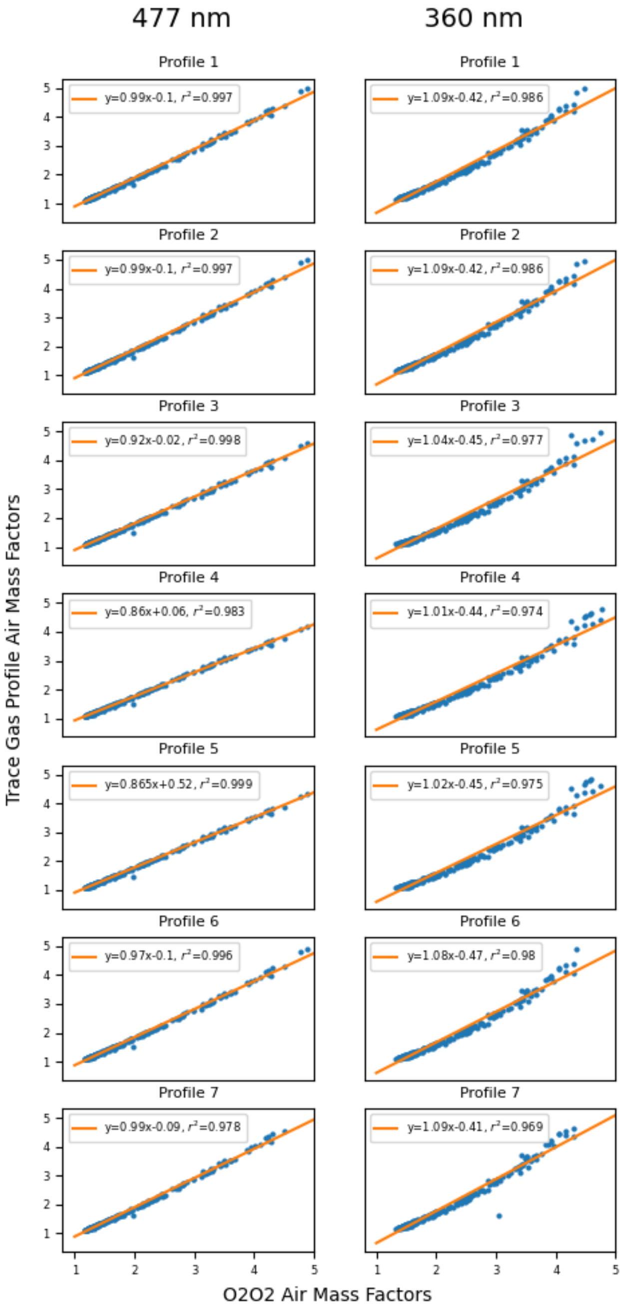

Figure 8. Linear fits of the AMFs retrieved from the seven profiles and the AMFs retrieved from the O_2O_2 profile at 360 nm(column a) and 477 nm(column b)

This method of AMF estimation could still be particularly useful for Mobile DOAS measurements in heterogeneous environments where the mobile lab might pass close to many sources where the NO_2 vertical profile will change continuously. Rather than attempting to estimate the NO_2 profile of every source, it is much simpler and a much more effective reduction of AMF uncertainty to simply estimate the O_2O_2 profile, since it is not influenced significantly by anthropogenic emissions in the way NO_2 is.

2.5.1 Trace gas amount in the reference spectrum: SCD_{ref}

In order to estimate the amount of NO_2 and HCHO in the reference spectrum, Langley extrapolation method was used on the morning data collected during September 22. Note, that the conditions at the Texas City dike (September 21) were not completely pollution free, but the next day was overall low pollution. Langley Extrapolation method (to zero AMF) assumes that a constant total column was present during the measurement period and a linear relationship exists between $\Delta SCD(gas)$ and $AMF(gas)$. The Langley plots can be seen in Figures A1 A2, and A3.

The reference AMFs were estimated using radiative transfer simulations as described above and limited to 2.2–4.2 SCD_{ref} derived from the Visible NO_2 retrieval was found to be 6.17×10^{15} $molecules\ cm^{-2}$ and the UV retrieval was found to be 4.28×10^{15} $molecules\ cm^{-2}$, with an estimated error of 0.79×10^{15} $molecules\ cm^{-2}$ and 1.21×10^{15} $molecules\ cm^{-2}$, respectively. The SCD_{ref} for HCHO was found to be 4.51×10^{15} $molecules\ cm^{-2}$ with an estimated error of 4.24×10^{14} $molecules\ cm^{-2}$

The stratospheric column is estimated from a climatology based on instrument latitude, the time of day, and season (Brohede et al., 2007). The climatology is provided as part of the standard Pandora data product, and the uncertainty is estimated at 1.35×10^{15} $molecules\ cm^{-2}$.

2.6 Error Estimation

When assessing the error incurred during the DOAS process, there are three main sources of error. These include the retrieval uncertainty, the AMF error, and the error arising from the estimation of the reference column. These error sources contribute to the final error estimation according to Equation 6 from (Tack et al., 2015). In addition, NO_2 has an additional source of error that arises due to the estimation of the stratospheric component of the vertical column that is not present for HCHO:

$$\sigma_{VCD}^2 = \left(\frac{\sigma_{\Delta SCD}}{AMF}\right)^2 + \left(\frac{\sigma_{ref}}{AMF_{ref}}\right)^2 + \left(\frac{SCD}{AMF} \cdot \frac{\sigma_{AMF}}{AMF}\right)^2 \tag{6}$$

Where $\sigma_{\Delta SCD}$ represents the uncertainty of the DOAS retrieval, σ_{ref} the uncertainty of the estimation of the reference column, and σ_{AMF} is the uncertainty of the AMF estimation.

Errors relating to the DOAS retrieval were included in the results of each individual fit, provided by QDOAS, and were a median of 5.80×10^{14} $molecules\ cm^{-2}$ for NO_2 Visible retrievals, 9.67×10^{14} $molecules\ cm^{-2}$ for NO_2 UV retrievals, and 4.24×10^{15} $molecules\ cm^{-2}$ for HCHO. The error arising from the estimation of AMFs is primarily due to errors in assumptions about the aerosol properties measured by the mobile lab, as well as assumptions of the vertical profile. An uncertainty factor of 20% of each AMF has been estimated from the results of sensitivity study presented in Section 3. This uncertainty translates to an estimated VCD error due to the AMF of 1.34×10^{15} $molecules\ cm^{-2}$ for the Visible NO_2 retrieval, 1.23×10^{15} $molecules\ cm^{-2}$ for the UV NO_2 retrieval, and 1.77×10^{15} $molecules\ cm^{-2}$ for HCHO. In addition, the error from the estimation of the residual trace gas measured by the reference spectrum arises predominantly from variations between the data used for the linear fit and fitted points themselves performed for Langley extrapolation. The difference between the real and extrapolated data was found to be 8.69×10^{14} $molecules\ cm^{-2}$ and 1.31×10^{15} $molecules\ cm^{-2}$, respectively for the NO_2 Visible and UV reference columns,and 4.24×10^{14} $molecules\ cm^{-2}$ for the HCHO reference column. Finally, the error from the estimation of the stratospheric component of the vertical column was taken from the standard deviation of the climatological stratospheric NO_2 column at a latitude of 29.75°, with median errors 7.93×10^{14} $molecules\ cm^{-2}$ for Visible and 7.23×10^{14} $molecules\ cm^{-2}$ for UV NO_2 stratospheric columns.

In order to estimate the effect of the error estimations on the final VCDs, each error source is shown in Table 4 as a percentage of the median VCD of NO_2, 6.23×10^{15} $molecules\ cm^{-2}$ and 3.51×10^{15} $molecules\ cm^{-2}$ for Visible and UV retrievals, respectively, and HCHO, 8.82×10^{15} $molecules\ cm^{-2}$.

Table 4. Summary of Error Sources for Visible NO_2 and HCHO VCDs

Trace Gas	$\sigma_{\Delta SCD}$	σ_{ref}	σ_{AMF}	σ_{strat}	σ_{Total}
NO_2 Visible	9.3%	13.9%	21.4%	12.7%	31.0%
NO_2 UV	27.6%	37.4%	35.1%	20.8%	65.7%
HCHO	47.8%	32.2%	19.9%	N/A	64.5%

3 Results

During September 2021, the Pandora instrument was active for 24 days of the month. Measurements were not taken from September 13 to September 16 due to a category 1 hurricane moving over Houston, in addition, the instruments were housed inside the mobile lab's garage for protection, and did not record measurements. On the 2nd, 4th, 6th, 17th, 18th, 19th, 22nd, and the 28th of September, the mobile lab was parked at the La Porte Municipal Airport (29.6698N, -95.0595W), east of the center of Houston and southwest of the Houston Ship channel. This is a small airport which does not see heavy air traffic but is close to multiple emission sources both to the north and south.

This section presents the mobile and stationary Zenith DOAS VCDs measured during TRACER-AQ onboard the Mobile Air Quality Lab 1 (MAQL1), while highlighting the relationship between Zenith DOAS columns and in situ surface concentrations observed during the field campaign. In particular, this relationship between surface and column is explored in more detail through two case days, and is used to provide further context to the trace gas emissions that contributed to two O_3 episodes that occurred during the field campaign.

https://doi.org/10.5194/egusphere-2025-5179
Preprint. Discussion started: 19 February 2026

3.1 Tropospheric NO_2 and HCHO Observed during TRACER-AQ

Figure 9 shows the time series of NO_2 Vertical Column Densities day by day for the month of September where the measured in situ NO_2 concentrations are plotted in black. On most days the NO_2 VCD remains between $0.5–2 \times 10^{16}$ $molecules\ cm^{-2}$, with high measurements reaching peaks of about 4×10^{16} $molecules\ cm^{-2}$.These values agree well with previous studies performed in Houston (Johansson et al., 2014; Rivera et al., 2010) as well as in Mexico City (Johansson et al., 2009). These values are higher than those found in Europe (Wagner et al., 2010; Constantin et al., 2013) but lower than those found in major Chinese cities (Wang et al., 2012; Huang et al., 2020). Due to the high level of uncertainty associated with the UV NO_2 data product, all data shown in the case studies section are Visible NO_2 products only.

Many of the peaks in NO_2 VCDs also coincide with peaks of O_2O_2, which suggest these peaks are the result of path length enhancements due to clouds (Platt et al., 1997). In particular, September 1,2, and 3 had significant enhancement of the O_2O_2 ΔSCDs in the early afternoon as can be seen in Figure A4. In order to correct for cloudy conditions the data was screened for clouds using a color index comparing the radiance measured at 320 nm to 440 nm and the temporal smoothness of the color index to filter small, scattered and optically thin clouds, and the differential AMF of O_2O_2(Wagner et al., 2014) to filter optically thick clouds. To screen for clouds, a clear sky reference was developed for comparison. This reference was developed from measurements made between September 22–26, a period of five days with no significant deviations of the O_2O_2 ΔSCDs. The clear sky reference was converted from individual date-times to each measurement's solar zenith angles and grouped accordingly. The clear sky reference was then interpolated to the solar zenith angle of each measurement, which gives the expected clear sky reference at each measurement's solar position. Color index values, after normalization to the reference, less that 0.5 with a temporal smoothness indicator, normalized to each measurement period, less than $1 \times 10^{-5} s^{-1}$, were flagged as optically thin or scattered clouds and removed from the dataset. In addition, measurements where the differential Air Mass Factor(dAMF) of O_2O_2, normalized to the clear sky reference, was less than 0.8 were flagged as optically thick clouds and removed from the dataset.

HCHO, on the other hand, is much more well mixed during the field campaign than NO_2. This is largely due to the production of HCHO, especially in Houston's urban core and surrounding industrial sites where the Pandora spent most of the month driving through, being produced by secondary formation from other VOCs emitted by Houston's oil refining and plastic production industries. Near sources of both VOCs and HCHO, the HCHO VCDs peak to $4–5 \times 10^{16}$ $molecules\ cm^{-2}$ with typical values ranging between $1–3 \times 10^{16}$ $molecules\ cm^{-2}$. In addition, some of the peaks in the HCHO VCD are not seen by the surface measurements, and vice versa. For example, on September 9, the HCHO VCD from 13:00 to 15:00 CDT peaks at multiple points to 4.5×10^{16} $molecules\ cm^{-2}$, however during this period there was no increase in the HCHO surface concentration; in fact, the surface concentration showed a gradual decreasing trend over this period with no short term increase in concentration while the HCHO VCDs were spiking.

https://doi.org/10.5194/egusphere-2025-5179
Preprint. Discussion started: 19 February 2026

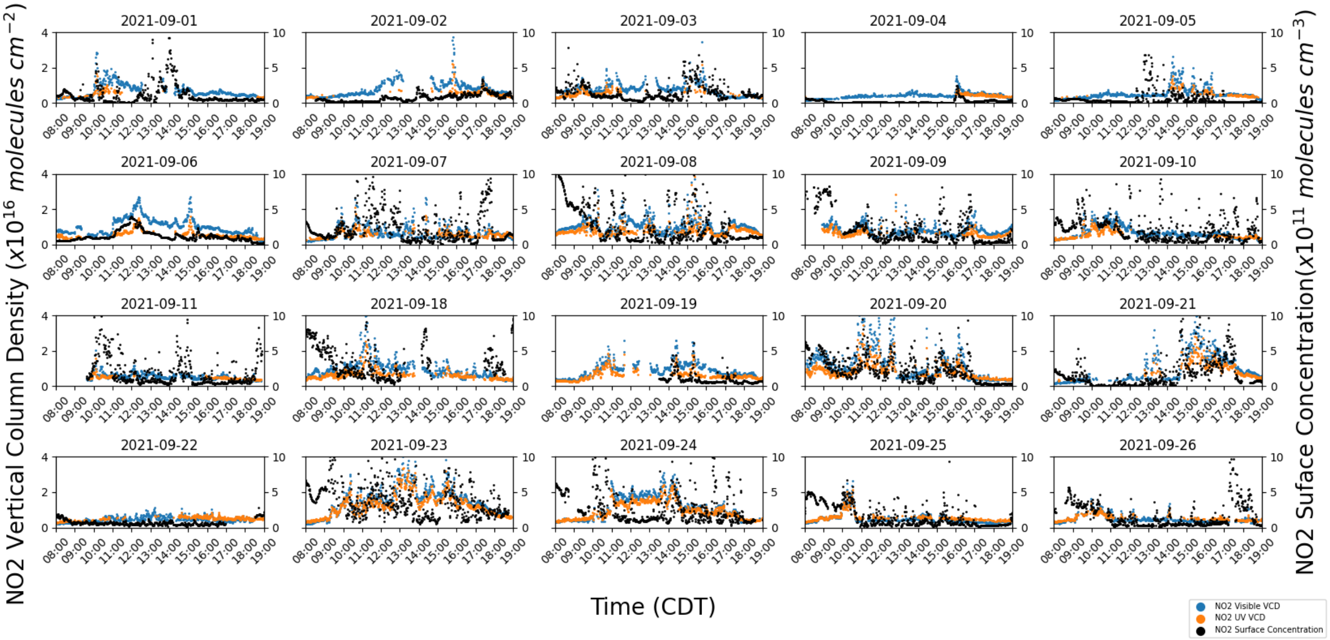

Figure 9. Time series of NO_2 VCDs for the month of September, separated by day and averaged every minute. The colored points represent retrieved NO_2 at the UV and VIS wavelengths, and the black points represent the measured NO_2 in situ concentration.

3.2 Case Studies

At many points during the field campaign, both in situ and Zenith DOAS measurements show good correlation when the instruments pass in proximity to a major source, such as on September 6 and 19 for NO_2, and September 23 and 25 for HCHO. This behavior indicates that the total vertical trace gas column is often influenced by trace gas conditions at the surface. However, there are often periods when one of the measurements sees a large increase in trace the other does not, such as on September 9 and 18, where the HCHO VCD rapidly increases with no corresponding increase in in situ concentration. This behavior shows that the ability of surface measurements and vertical columns to agree is based on how related the entire trace gas vertical distribution is to the surface conditions. While the vertical column densities and the in situ concentrations measured describe different concentrations at different altitudes, they can be combined to give further information on the distribution of trace gas directly overhead both instruments. By comparing the two measurement quantities, the ratio between the two can be determined which corresponds to an altitude representing an estimated pseudo-mixing layer height of the trace gas. The CSR can be compared to estimations of the true mixing layer height retrieved from ceilometer measurements to approximate the vertical distribution of the trace gas measured and estimate whether the majority of the trace gas is located close to the surface, elevated below the mixing layer height, or well mixed within the mixing layer. While the CSR will not have as much information on the vertical profile than profiles retrieved from a sky scan, CSRs can be measured at a much faster rate, being only limited by the time it takes to take a single measurement. This makes the CSR a more desirable quantity when

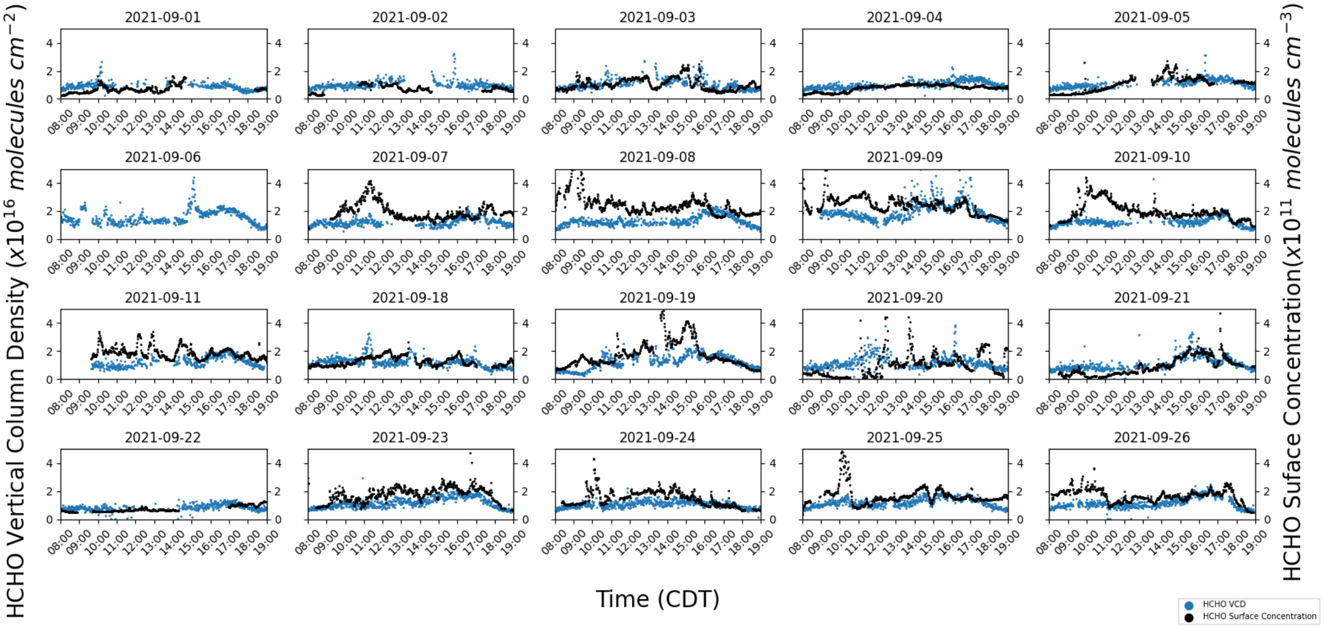

Figure 10. Time series of HCHO VCDs for the month of September, separated by day and averaged every minute. The colored points represent the retrieved HCHO VCD, and the black points represent the measured HCHO in situ concentration.

the air masses being measured can significantly change over short periods of time, as is the case for mobile measurements. This behavior can be used to separate trace gas from elevated transport patterns, such as plumes, from local emissions, such as vehicles, emissions related to airports, and provide further context into the underlying chemical processes of trace gases observed by other instruments, namely the formation of O_3.

Figure A5 shows the CSRs of NO_2 found using the 1 minute averages measurements of in situ and Pandora data collected during TRACER-AQ, during the month of September. Typical values range from in the 10s of meters, representing NO_2 columns influenced by vehicular emissions, to up to 2 km, representing elevated columns of NO_2. While the mobile lab remained stationary, typically CSRs were characterized consistent value close to 800 m for NO_2, representing well mixed columns as can be seen on most mornings. However, while the mobile lab traveled around the Houston area the CSRs can quickly shift between surface and elevated regimes as many sources on the surface, such as industry and traffic congestion, are seen by the instruments.

HCHO, on the other hand, is a more well mixed trace gas than NO_2 and as such will show fewer variations, both while the mobile lab travels and remains stationary. Figure A6 shows the CSRs found by comparing 1 minute averages of both Pandora and in situ measurements. Typical CSRs for HCHO are around 1–3 km, however there are also periods when the ratio increases to upwards of 5 km, indicating large quantities of HCHO elevated well above the surface.

This behavior is especially clear on September 6, which is one of the days that the mobile lab remained parked at La Porte Regional Airport. Starting at 10:50 CDT the NO_2 VCD increased from $0.5 - 1.5 \times 10^{16}$ $molecules\ cm^{-2}$, with the in situ

430 measurements lagging by approximately 20 minutes, when surface concentrations rose from 1–2 $\times 10^{11}$ $molecules\ cm^{-3}$. This leads to a short increase in the CSR to 1.2 km before the surface concentrations caught up to the VCD measurements, after which the CSR reduced back to approximately 500 m, indicating the observed NO_2 in the direct vicinity of the airport is well mixed vertically, and any additional NO_2 transported into the measurement area mixes over time as well.

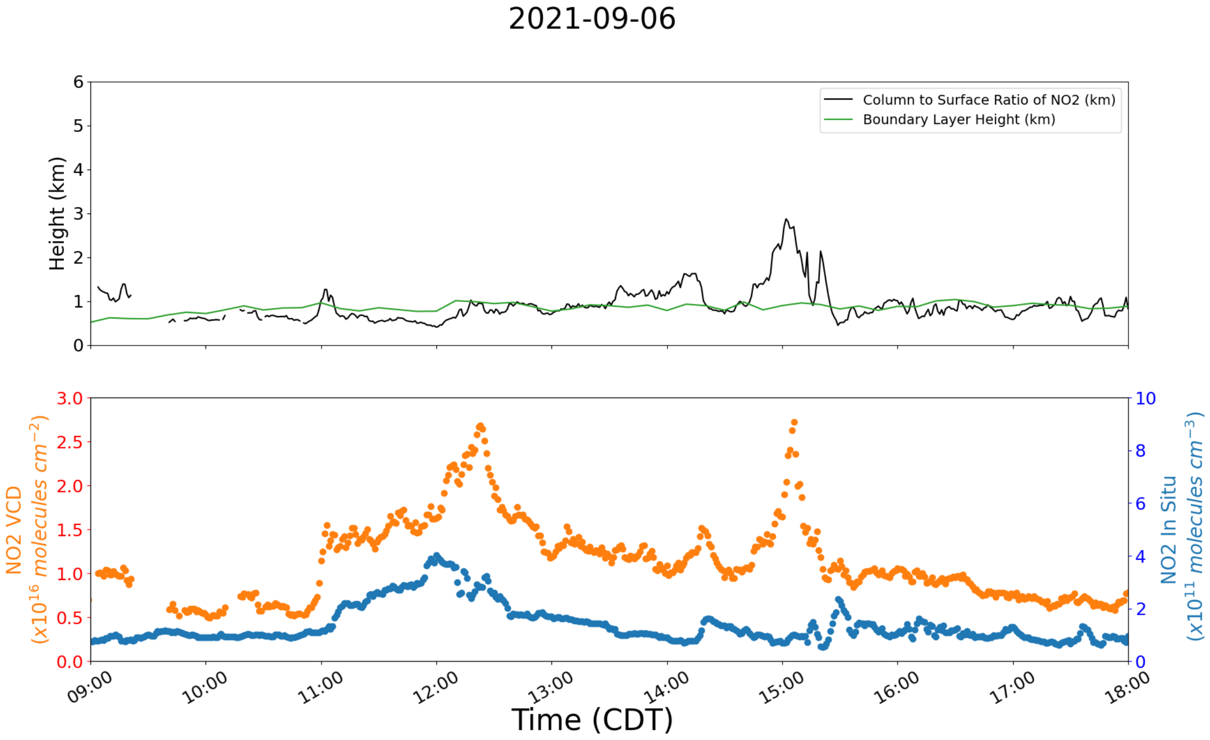

Figure 11. Time series of NO_2 VCD, in situ concentration one minute averages(b), as well CSR, in black, and boundary layer height, in green(a) for September 6. Aside from the boundary layer height, which is the diurnal variation averaged every 10 minutes, all data shown is presented as 1 minute averages.

Of particular interest on the 6th is the time between 14:00 and 17:00 CDT, when local O_3 monitors on the mobile lab 435 detected an O_3 episode, where the mean O_3 concentration remained above 20×10^{11} $molecules\ cm^{-3}$ during the period. This time period corresponds with two spikes in the CSR, one at 14:30 and another at 15:00. This first spike corresponds to a small increase in both the NO_2 VCD from 1–1.5 $\times 10^{16}$ $molecules\ cm^{-2}$ as well as the surface concentration, from 0.8–1.8 $\times 10^{11}$ $molecules\ cm^{-3}$. However, due to the CSR already remaining elevated for the previous hour, only a small change in the CSR occurs, from 600 m–1.5 km. On the other hand, the second spike in the CSR is entirely due to a large increase in the NO_2 VCD, 440 from 1–2.5 $\times 10^{16}$ $molecules\ cm^{-2}$ with no corresponding change in the in situ surface concentration, resulting in an increase in the NO_2 CSR from 600 m–2.5 km. Both of these instances indicate the presence of large quantities of elevated NO_2 being transported into the area around the airport during the O_3 episode, likely the result of plumes from nearby emissions sources.

https://doi.org/10.5194/egusphere-2025-5179
Preprint. Discussion started: 19 February 2026

In addition, while there is no corresponding in situ measurements on the 6th for HCHO in order to perform this analysis, the HCHO VCD increases from $1.5–4 \times 10^{16}$ $molecules\ cm^{-2}$ at 13:00 CDT, matching the observations of NO_2 while there is no 445 significant increase in HCHO at 14:30. Therefore, it is likely that the second plume included not just NO_2 but HCHO as well, two well known tracers for O_3 production.

In order to determine the origin of the observed plumes, the Hybrid Single-Particle Lagrangian Integrated Trajectory (HYSPLIT)(Stein et al., 2015) was used to simulate back-trajectories of the air masses observed during the O_3 episode. Figure A8 shows four back-trajectories from 16:00 CDT (red) to 13:00 CDT (cyan). Based on the modeled trajectories, during the O_3 450 episode the air masses measured transported largely from the north and northeast directions. In particular, the area directly north of the small inlet that all four trajectories cross corresponds to one of the largest petrochemical refining complexes in the city. This is a potential cause of the increases in both NO_2 and HCHO observed: large amounts of VOCs and NO_x are produced at refineries, and as such after spending more than an hour transporting south to the airport, a portion of both trace gas groups had both reacted to form NO_2, HCHO, which continued to mix at the airport to cause the O_3 episode observed on this day.

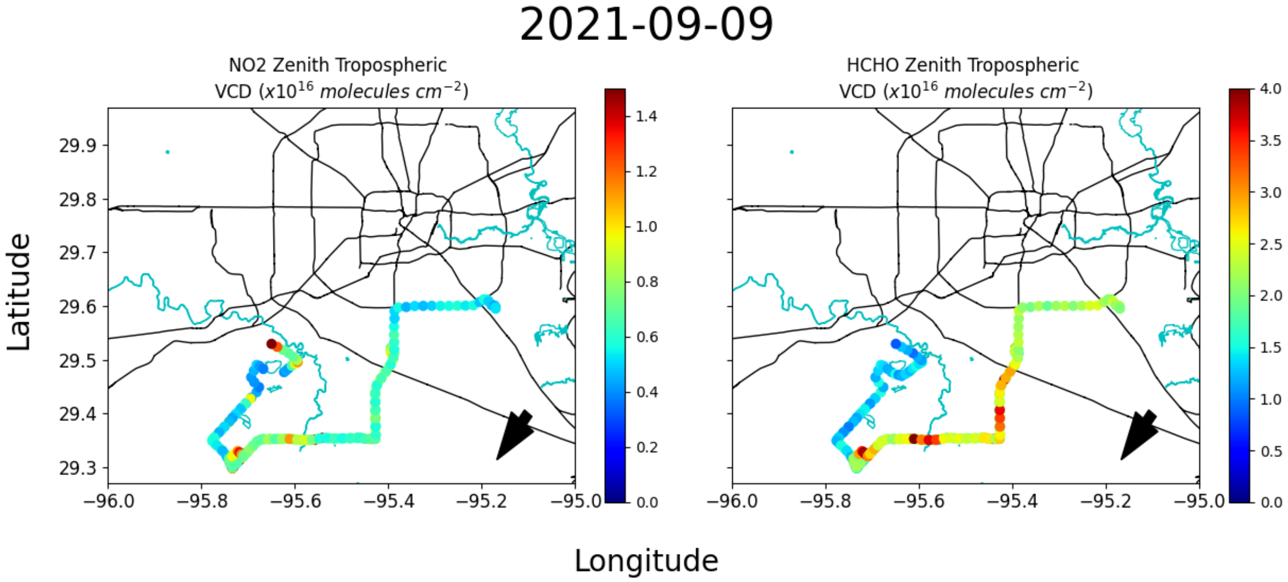

Figure 12. The driving route of MAQL1 on September 9 during the locally observed O_3 episode. In addition, the maps show the Zenith NO_2(a) and HCHO(b) VCDs retrieved during this time frame. The arrows in the bottom right of each plot shows the average wind direction collected from 5 airports located in the vicinity of the driving path. The average wind speed during this period was 3.56 m/s. All data shown is presented as 1 minute averages.

455 On September 9 the mobile lab was driven around the suburban and rural areas to the direct south of Houston's urban core, with the map of the measurements during the O_3 episode shown in Figure 12, and map of the full driving route shown in Figure A9. This route differs from most of the routes traveled during TRACER-AQ in that the mobile lab did not travel close to any major industrial centers, and instead had the opportunity to measure longer range transport away from both the urban

core and industrial sites. Between 11:30 to 15:30, an extended O_3 episode occurred, with surface O_3 concentrations remaining consistently around 20×10^{11} $molecules\ cm^{-3}$ during the four hour period. The region the mobile lab was in during this period is shown in Figure 12.

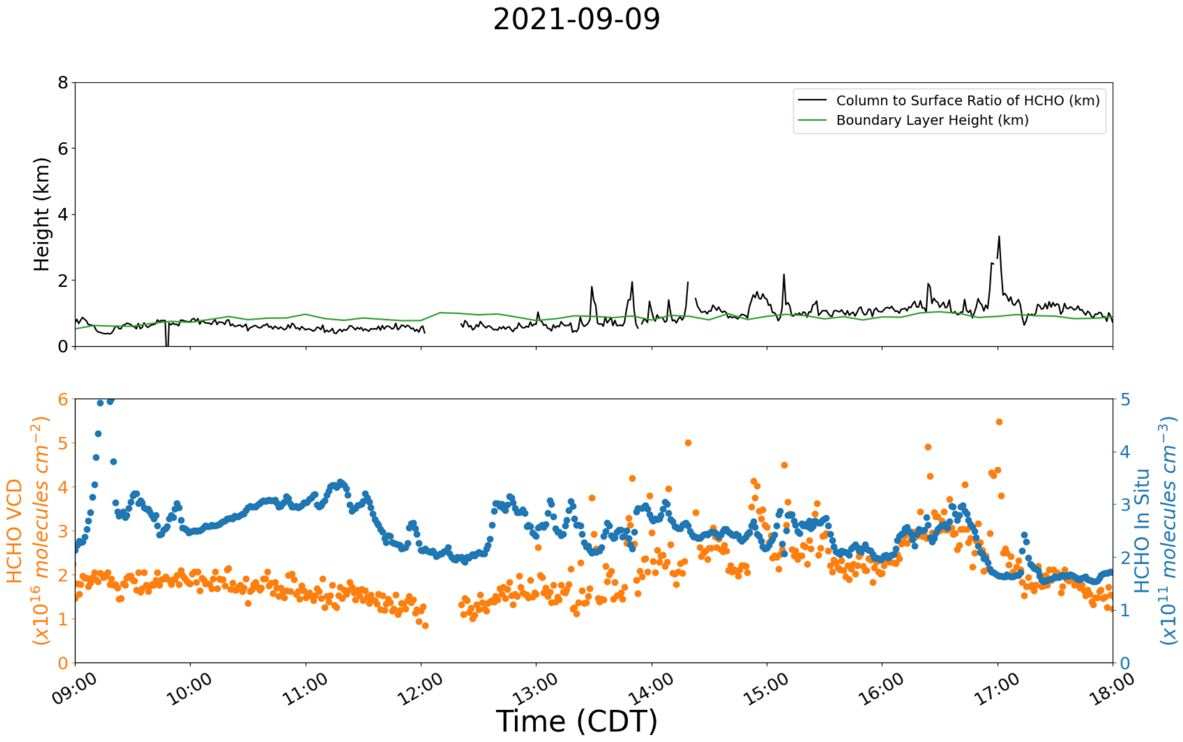

Figure 13. Top: The CSR of HCHO (black) and corresponding diurnal averaged Boundary Layer Height (green) on September 9. Bottom: The HCHO Tropospheric Vertical Column Density (red) and the in situ surface concentration (blue). Aside from the boundary layer height, which is the diurnal variation averaged every 10 minutes, all data shown is presented as 1 minute averages.

Figure 13 shows the behavior of both the HCHO VCD and in situ concentration during this time. From 10:00 to 13:00 CDT the HCHO VCD remains consistent between $1–2 \times 10^{16}$ $molecules\ cm^{-2}$. This time period corresponds with the mobile lab traveling further out of the Houston metropolitan area and into a more rural region. In addition, during this O_3 episode, as well as directly preceding a smaller event from 17:00 to 17:40 CDT, there are multiple spikes in the HCHO VCD between $4–5 \times 10^{16}$ $molecules\ cm^{-2}$ that are not present in the in situ surface concentration. However, during the entire day the surface concentration remains elevated between $1–3 \times 10^{11}$ $molecules\ cm^{-3}$, with a spike to 5×10^{11} $molecules\ cm^{-3}$ at around 9:10 CDT. This indicates that while the surface HCHO is well mixed , there are also elevated concentrations of HCHO also present. These increases in the HCHO VCDs are likely due to secondary formation of HCHO in these areas. Due to this secondary formation during the ozone episode, the CSR was more elevated when compared to the CSR values prior to the ozone episode, which suggests that most of the observed HCHO during the ozone episode was not interacting at the surface.

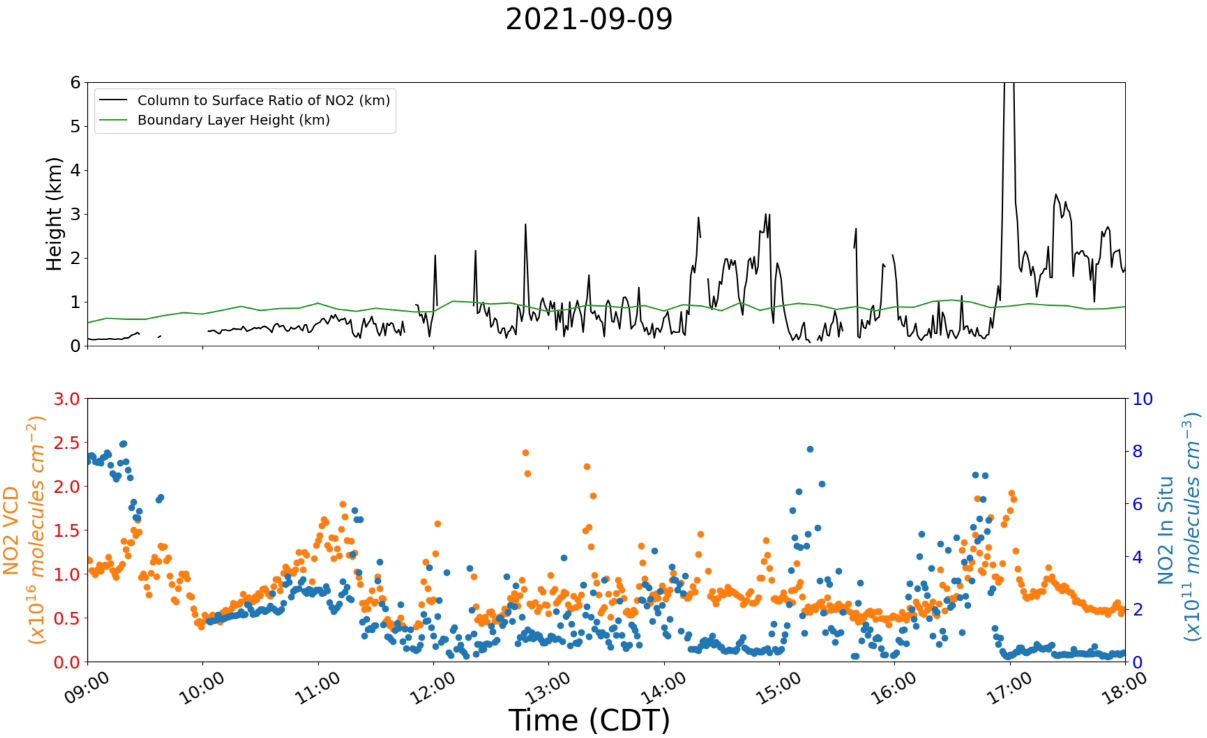

Figure 14. Top: The CSR of NO_2 (black) and corresponding diurnal averaged Boundary Layer Height (green) on September 9. Bottom: The NO_2 Tropospheric Vertical Column Density (red) and the in situ surface concentration (blue). Aside from the boundary layer height, which is the diurnal variation averaged every 10 minutes, all data shown is presented as 1 minute averages.

NO_2 saw a large increase of $0.5–1.5 \times 10^{16}$ $molecules\ cm^{-2}$ between 10:00 and 11:00 CDT as the instruments began to travel out of the urban core, but quickly dropped to 0.5×10^{16} $molecules\ cm^{-2}$. During the period of high O_3 many of the peaks seen in Figure 13 are also seen in Figure 14 such as at 13:30 and 15:00, which suggests that many of these elevated HCHO concentrations were plumes that carried both HCHO and NO_2. In addition, the NO_2 surface concentrations were influenced by on road emissions, with the NO_2 in situ concentrations for most of the day showing high variations, at times shifting between $0.5–8 \times 10^{11}$ $molecules\ cm^{-3}$. In spite of this, at many of the peaks in both HCHO and NO_2 the NO_2 surface concentration maintained a low and consistent value, which in turn resulted in CSRs well above the boundary layer in an elevated regime.

The behavior of both trace gases during the O_3 episode suggest that there are significant quantities of both HCHO and NO_2 being transported into the area and interacting with the HCHO already present. This behavior can also be seen in Figure A11, when lower local ozone levels were recorded. While the NO_2 VCDs on September 26 were higher in the same area of the ozone episode on September 9, background HCHO VCDs were between $1–1.5 \times 10^{16}$ $molecules\ cm^{-2}$, significantly less than on September 9, with no large increases in the same area where increases in HCHO were observed on September 9.

In order to determine the origin of these air masses, wind data was collected from five airports located near the driving path (Ellington Airport(29.6060, -95.1664), Houston Southwest Airport(29.5065, -95.4688), Pearland Regional Airport(29.5190, -95.2421), Sugar Land Regional Airport(29.6271, -95.6556), William P. Hobby Airport (29.6442, 95.2786)). These airports reported light winds between 0–5 $m\ s^{-1}$ from the northeast during the O_3 episode, with the average of these locations being 3.95 $m\ s^{-1}$ at 37.7°. This wind pattern indicates that the air masses likely originated from the urban core and industrial center of Houston.

3.3 Discussion

While MAX-DOAS is more than capable of performing sky scans to retrieve vertical profiles, it is not possible to perform a full sky scan on a moving vehicle: the air masses measured will change during the scan, affecting the measurements. However, while the Zenith DOAS viewing geometry is capable of a more rapid measurement schedule than MAX-DOAS it is too limited of a viewing geometry to describe vertical trace gas distributions. The addition of an in situ measuring instrument, as well as the calculation of the CSR, can add more information on the vertical distribution of trace gas. While the CSR does not provide as much information about the vertical trace as distribution as a full MAX-DOAS sky scan, this method does provide information on the vertical transport of trace gas within the region, and provide real-time validation of the Mobile-DOAS measurements.

The identification and quantification of pollution sources can be enhanced by knowing the CSR. For instance, instruments passing within the vicinity of industrial sources, such as petrochemical refineries which emit from flares or fossil fuel power plants which emit from smokestacks, can give the appearance of a CSR in an elevated or well mixed regime. This behavior deviates from typical CSRs based on on-road measurements, which are expected to be low due to the influence of vehicular emissions.

Calculation of emission fluxes requires a wind profile to accurately determine the transport of emissions in space and time, however prior emission flux papers that have been discussed in this paper assume a homogeneously distributed vertical column density due to the technique's inability to measure trace gas profiles. In lieu of a full profile, the CSR can be used to determine the relevant portions of the trace gas profile where wind measurements are most needed, to provide a more accurate flux measurement.

While most CSRs remain within reasonable estimations for the boundary layer height and the effect of elevated concentrations on in situ surface measurements, there are times that the height spikes to well above the boundary layer. For instance, in Figure A5 on September 1 at approximately 10:00 CDT the height spikes to around 10 km, well into the free troposphere. This is well beyond the upper limits of the boundary layer, and could be the result of cloud enhancement, not screened by the method used. Otherwise, this is an extreme example of an elevated concentration of NO_2, where in spite of consistent NO_2 VCDs, the lack of any measured concentration at the surface indicates that the NO_2 measured is entirely elevated and not interacting with the surface.

The sensitivity to one of the measured quantities is also enhanced when the other quantity is close to zero. This is also true of the same spike on September 1 at 10:00 CDT. not only is the VCD enhanced by clouds, but the low in situ concentrations cause the CSR to remain large both both before and after the cloud enhancement, albeit at a lower height. The opposite case can be seen on September 26 between 17:00 and 18:00 CDT, where the surface concentrations measured showed high variation between 1–10 × 10^{11} $molecules\ cm^{-3}$. On the other hand, the NO_2 VCD remains below 1×10^{16} $molecules\ cm^{-2}$, which is among the lowest VCDs measured during the field campaign. This result is likely due to the presence of vehicles nearby influencing surface concentrations, and leads to CSRs below 100 m, which is also among the lowest CSRs measured during the field campaign.

4 Conclusions

During TRACER-AQ 2021 tropospheric vertical column densities of NO_2 and HCHO were measured on a mobile lab as it traveled throughout Houston, Texas using the ZSL-DOAS remote sensing technique with collocated in situ instruments measuring local surface concentrations. The two quantities were used to determine the CSR, which is then used to estimate the vertical distribution of trace gas overhead the instruments, with low values representing a vertical distribution biased to the surface, higher values that remain below the boundary layer representing well mixed distributions, and high values well above the boundary layer height representing elevated distributions.

In addition, AMFs of Pandora Zenith measurements were estimated through radiative transfer measurements, based on averages of aerosol properties retrieved from 6 AERONET instruments installed in the Greater Houston Area. In order to estimate the uncertainty that averaging the aerosol properties introduce into the AMF estimations, three sensitivity studies were conducted in order to determine the contribution to AMF uncertainty due to: daily averaging of SSA and ASY, hourly averaging of AOD and aerosol profile, and the impact of a priori profile in the final AMF retrieval. All of these assumptions combined to approximately 15% uncertainty for visible AMF estimations, and 20% for UV AMF estimations.

NO_2 VCDs ranged between $1–2 \times 10^{16}$ $molecules\ cm^{-2}$ during the field campaign, with peaks reaching upwards of 5×10^{16} $molecules\ cm^{-2}$; this behavior is representative of previous ZSL-DOAS studies performed in Houston. On the other hand, HCHO columns ranged between 1–3 × 10^{16} $molecules\ cm^{-2}$ with peaks reaching 5×10^{16} $molecules\ cm^{-2}$, also matching previous studies performed in Houston as well as Mexico City.

Through analysis of the CSR, it is possible to determine the effects of local sources on the measurement area. For instance, On September 6, an O_3 episode was observed while the instruments were parked at la Porte airport. During the episode, two peaks in the NO_2 CSR, from 700 m to 1.5 km and 2.5 km, suggest that the increase in NO_2, as well as HCHO were due to transport of elevated concentrations of both trace gases, potentially from a major refinery complex directly North of the instruments. In addition, on September 9, multiple spikes in both the NO_2 and HCHO VCDs suggest that the trace gases driving local O_3 production were elevated, and likely transported from the urban core, which is located directly North of the instrument's area of operation at this time. These case studies demonstrate how future studies using mobile zenith DOAS measurements, with the addition of collocated in situ measurements, can be used to infer information about trace gas vertical distributions that that would not be available to either measurement technique alone. Especially in the context of a short term field campaign, this technique can help to understand how representative measurements from long term monitoring stations at the surface are of chemistry occurring aloft.

Code and data availability. BlickP (https://www.pandonia-global-network.org/home/documents/software/), libradtran (https://www.libradtran.org/doku.php?id=download), QDOAS (https://uv-vis.aeronomie.be/software/), and HYSPLIT (https://www.arl.noaa.gov/hysplit/) are all open source softwares available at the websites listed. All additional code for analysis and figure preparation was written in Python and is available on request. All data related to the TRACER-AQ field campaign can be found at the following data repository:tracer-aq data:https://www-air.larc.nasa.gov/cgi-bin/ArcView/traceraq.2021. All related AERONET data can be found at the following website: https://aeronet.gsfc.nasa.gov/. All intermediate data products are available on request.

Author contributions. DE and EL concieved the research idea. JF, TG, SU, SG provided provided ceilometer, in situ, other carbourne data, and operated all mobile instruments during the field campaign. DE performed the analysis and simulations, and wrote the initial draft. All authors contributed to the interpretation of results and preparation of the paper

Competing interests. The authors declare that they have no conflict of interest.

Acknowledgements. We would like to thank he organizers of the TRACER-AQ field campaign, as well as the other participants of the campaign. We would also like to thank James Flynn for his effort in establishing and maintaining the Aldine, Liberty, Sugarland the UH Coastal Research Center, and the University of Houston Main Campus sites, as well as Rick Wagener and Lynn Ma for their effort in establishing and maintaining the La Porte Airport site. We would also like to thank John Sullivan for his contribution of ozonesonde measurements during the TRACER-AQ field campaign.

Appendix A: Extra Figures

https://doi.org/10.5194/egusphere-2025-5179
Preprint. Discussion started: 19 February 2026

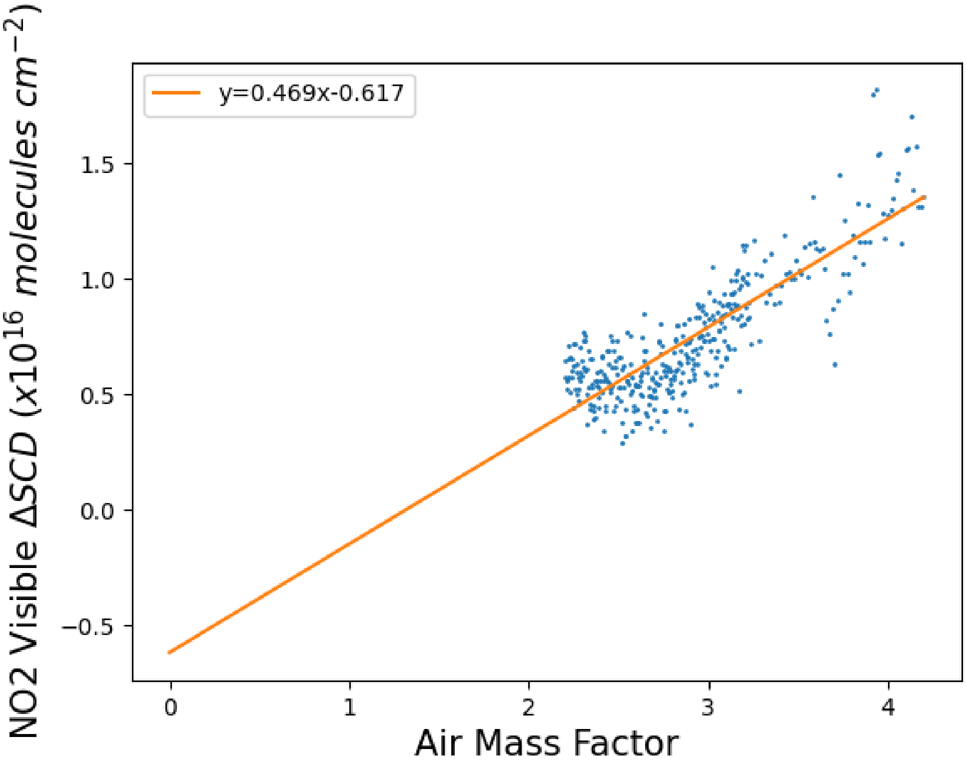

Figure A1. NO_2 differential slant column densities retrieved at 460 nm from measurements on the reference day, September 22, plotted as a function of the NO_2 AMFs retrieved at 460 nm from September 22. Each red dot represents the minimum ΔSCD in each bin which is used for a linear fit which is used for Langley Extrapolation is shown as a red line. The reference column of NO_2 was estimated to be 6.17×10^{15} $molecules\ cm^{-2}$

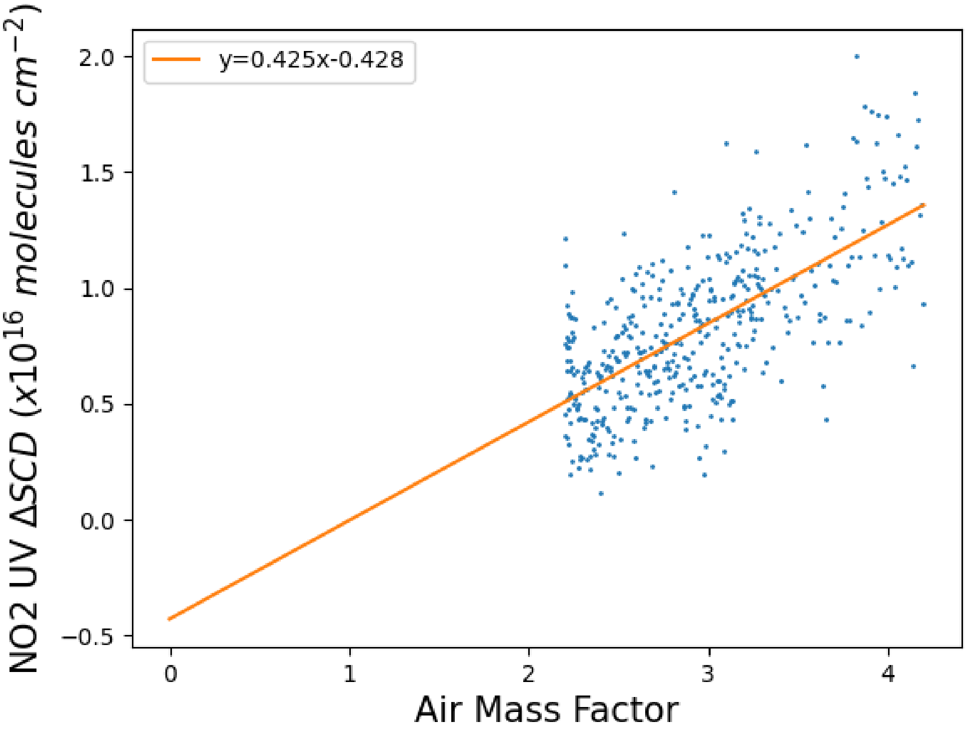

Figure A2. NO_2 differential slant column densities retrieved at 360 nm from measurements on the reference day, September 22, plotted as a function of the NO_2 AMFs retrieved at 360 nm from September 22. Each red dot represents the minimum ΔSCD in each bin which is used for a linear fit which is used for Langley Extrapolation is shown by the red line. The reference column of NO_2 was estimated to be $4.28 \times 10^{15}\ molecules\ cm^{-2}$

https://doi.org/10.5194/egusphere-2025-5179
Preprint. Discussion started: 19 February 2026

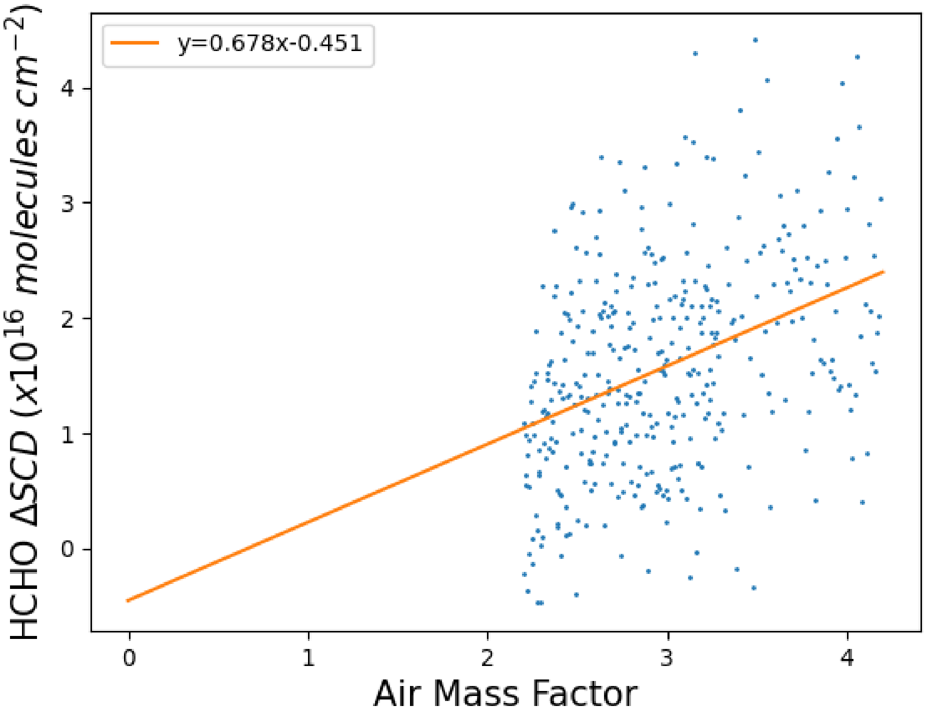

Figure A3. HCHO differential slant column densities retrieved at 340 nm from measurements on the reference day, September 22, plotted as a function of the HCHO AMFs retrieved at 340 nm from September 22. The linear fit which is used for Langley Extrapolation is shown as a red line. The reference column of HCHO was estimated to be $4.51 \times 10^{15}\ molecules\ cm^{-2}$

https://doi.org/10.5194/egusphere-2025-5179
Preprint. Discussion started: 19 February 2026

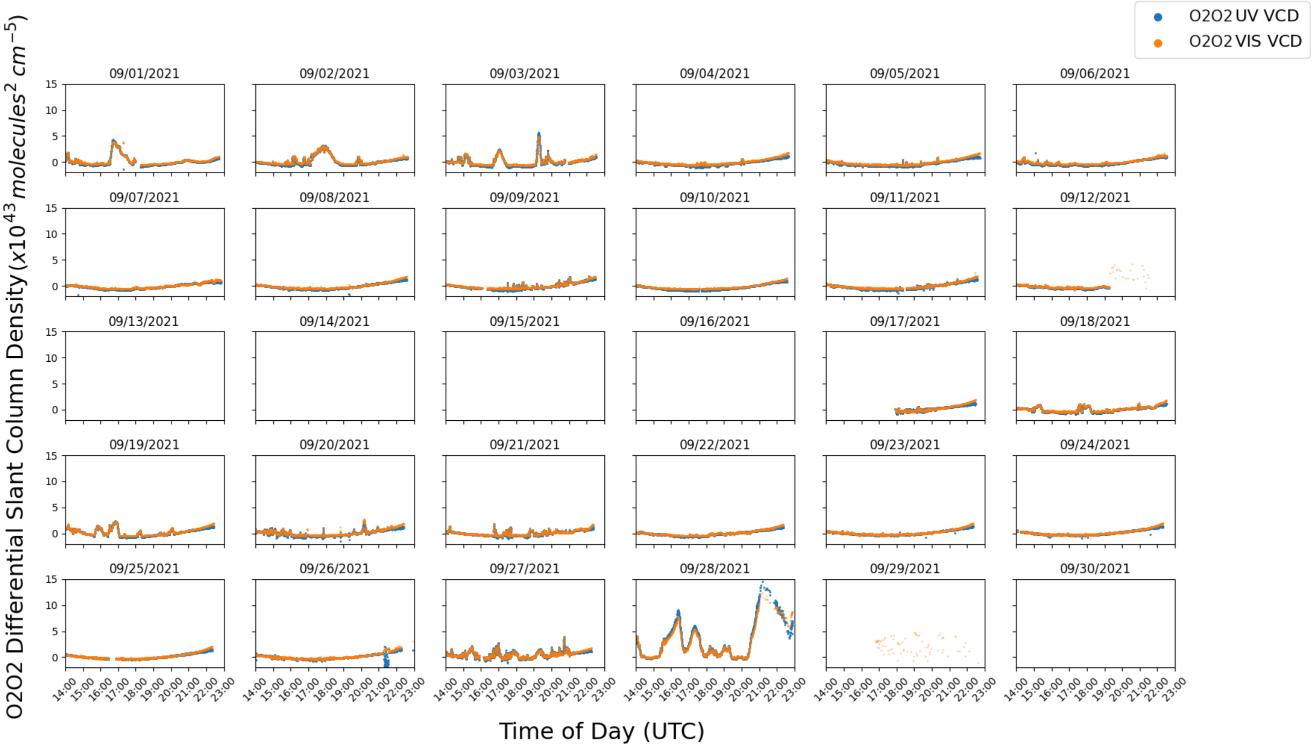

Figure A4. Time series of the O_2O_2 differential Slant Column Density for the month of September retrieved for both UV and VIS fitting windows.

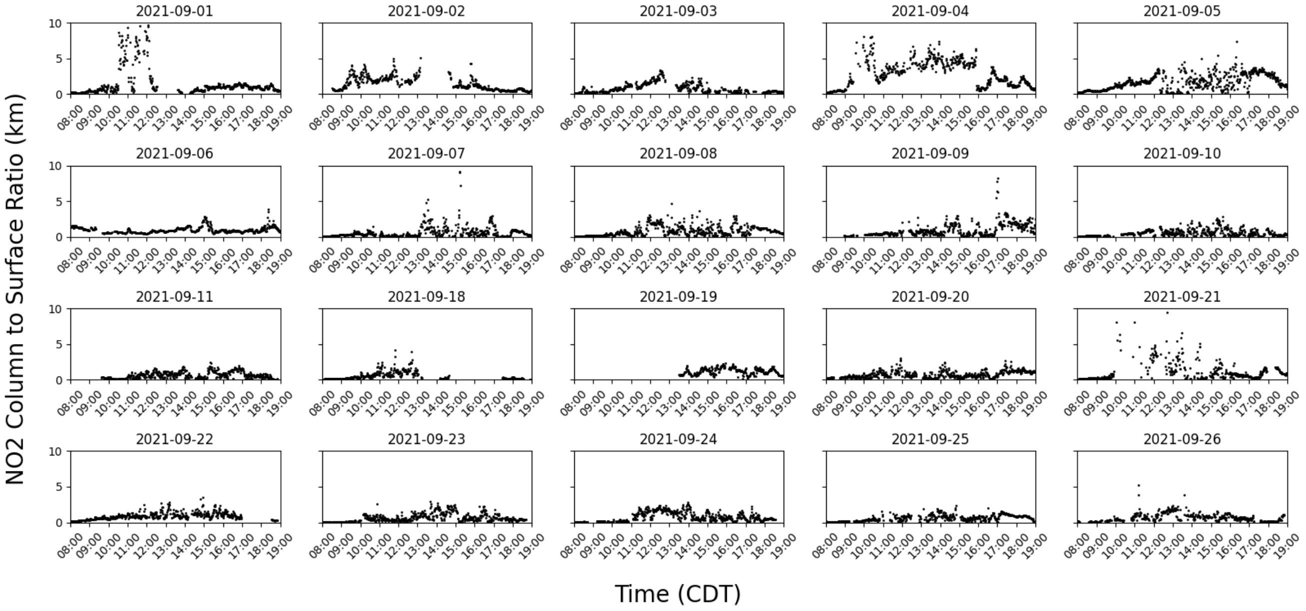

Figure A5. Time series of NO_2 CSRs for the month of September. All data shown is presented as 1 minute averages.

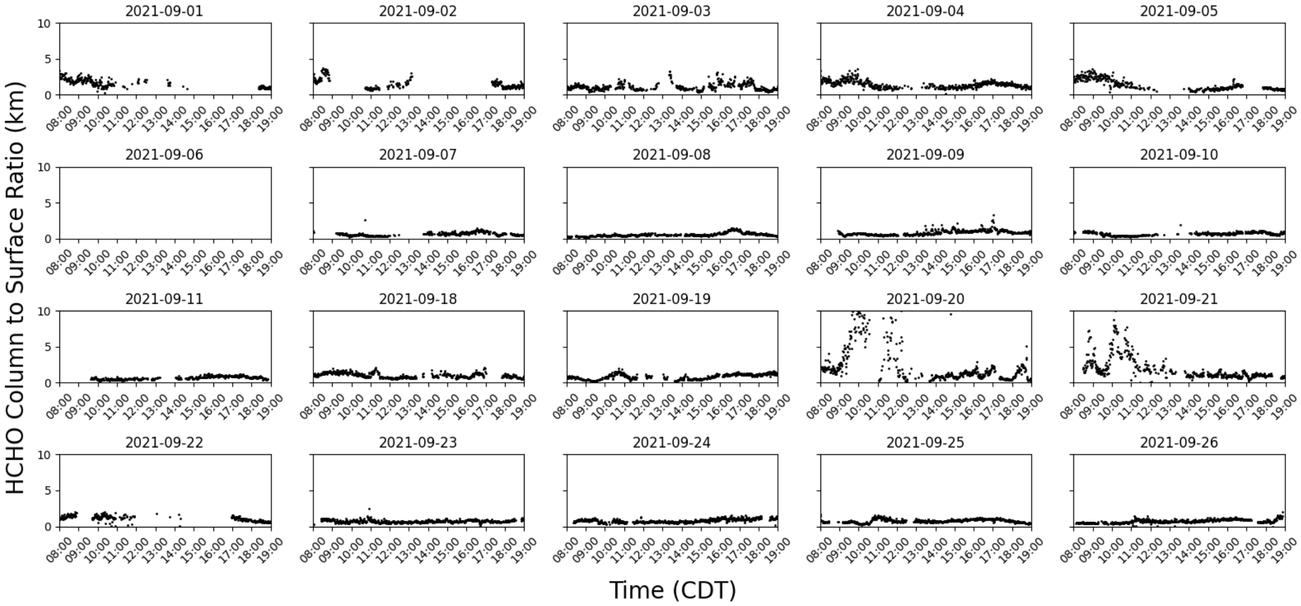

Figure A6. Time series of HCHO CSRs for the month of September. All data shown is presented as 1 minute averages.

https://doi.org/10.5194/egusphere-2025-5179
Preprint. Discussion started: 19 February 2026

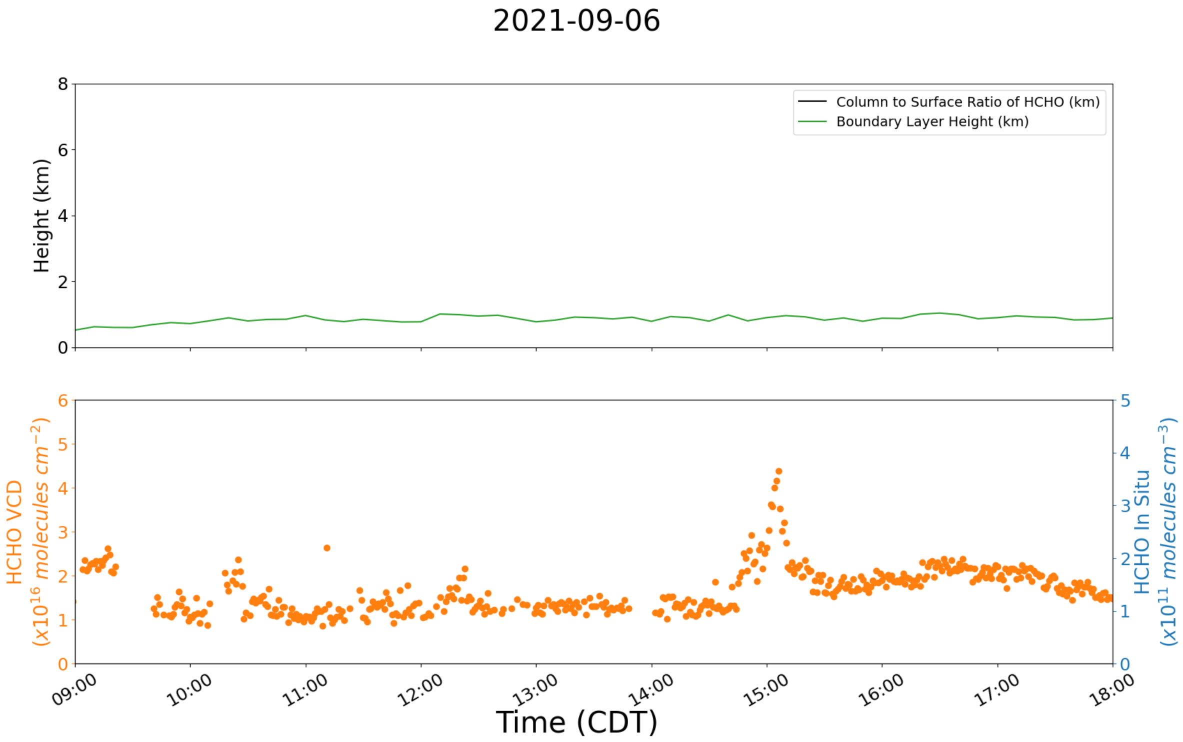

Figure A7. Top: The diurnal averaged Boundary Layer Height (green) on September 9. Bottom: Time series of HCHO VCD on September 6. Due to the absence of in situ measurements on this day, there is no CSR values to report. Aside from the boundary layer height, which is the diurnal variation averaged every 10 minutes, all data shown is presented as 1 minute averages.

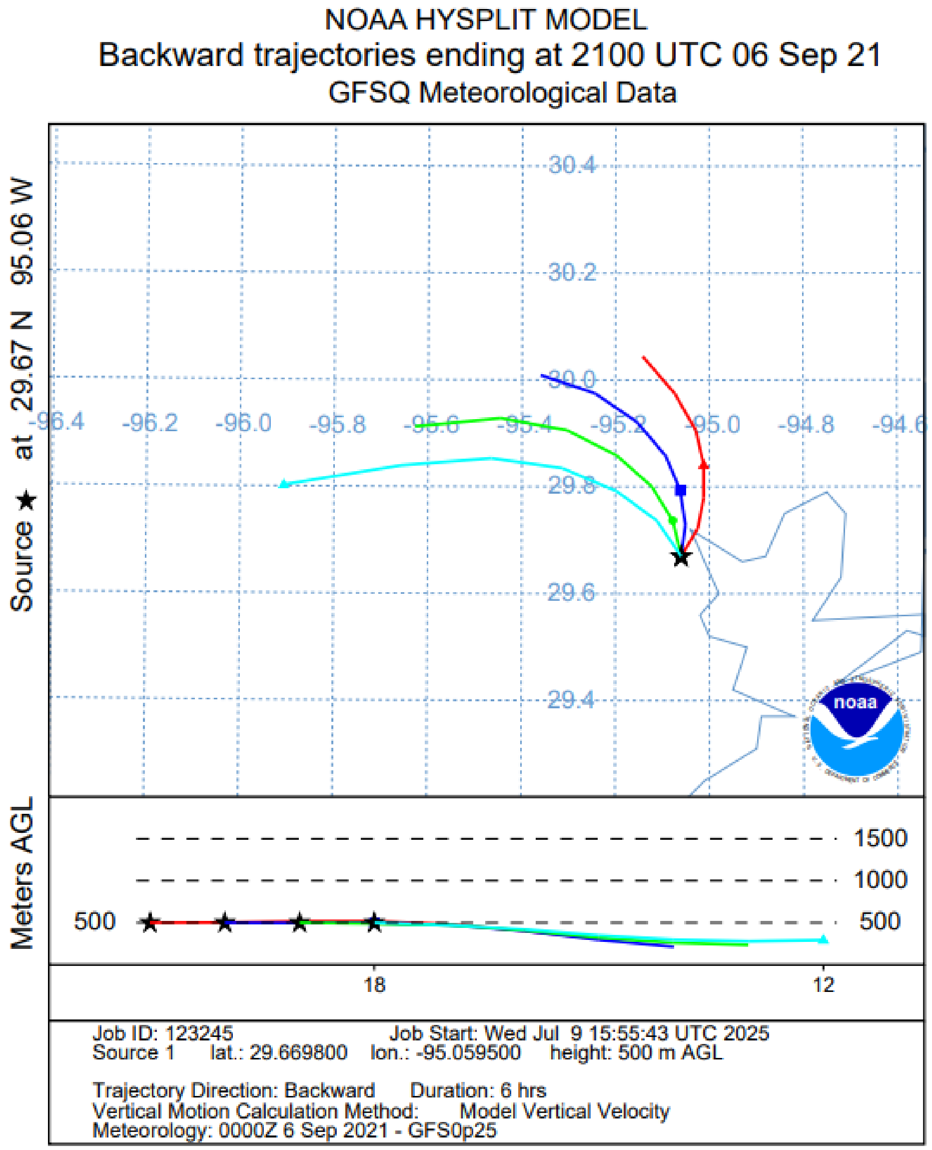

Figure A8. HYSPLIT (Stein et al., 2015) modeled 3 hour back-trajectory showing the path air masses at 17:00 (red), 16:00 (blue), 15:00 (green), and 14:00 (cyan) took to arrive at the la Porte Airport (starred).

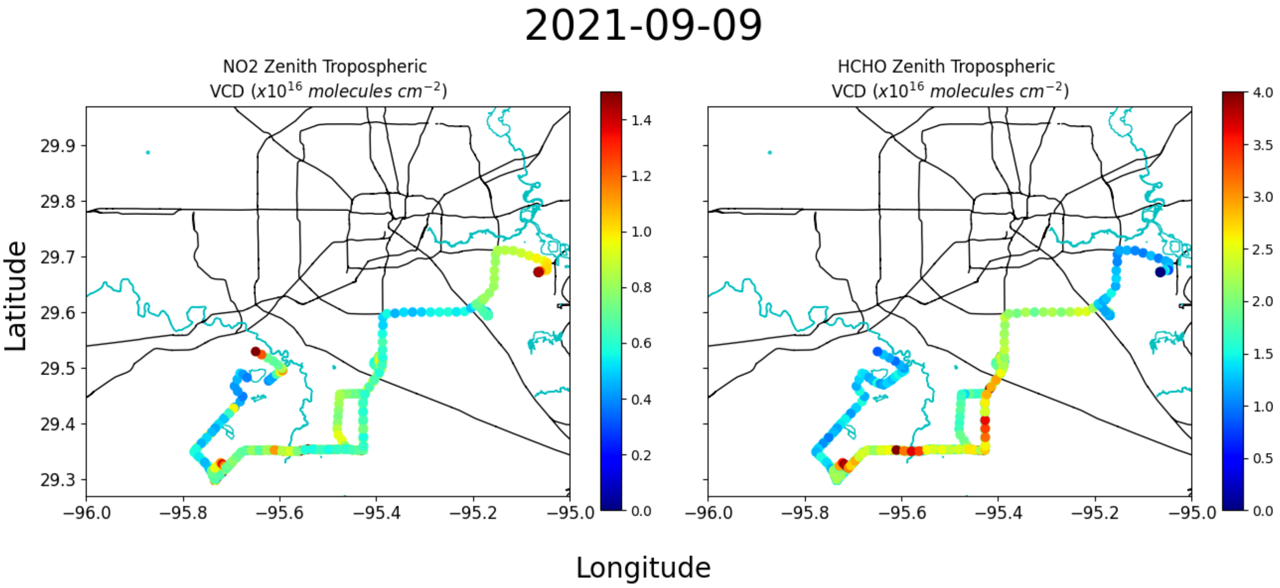

Figure A9. The full driving route of MAQL1 on September 9. In addition, the maps show the Zenith NO_2(a) and HCHO(b) VCDs retrieved during this time frame. All data shown is presented as 1 minute averages.

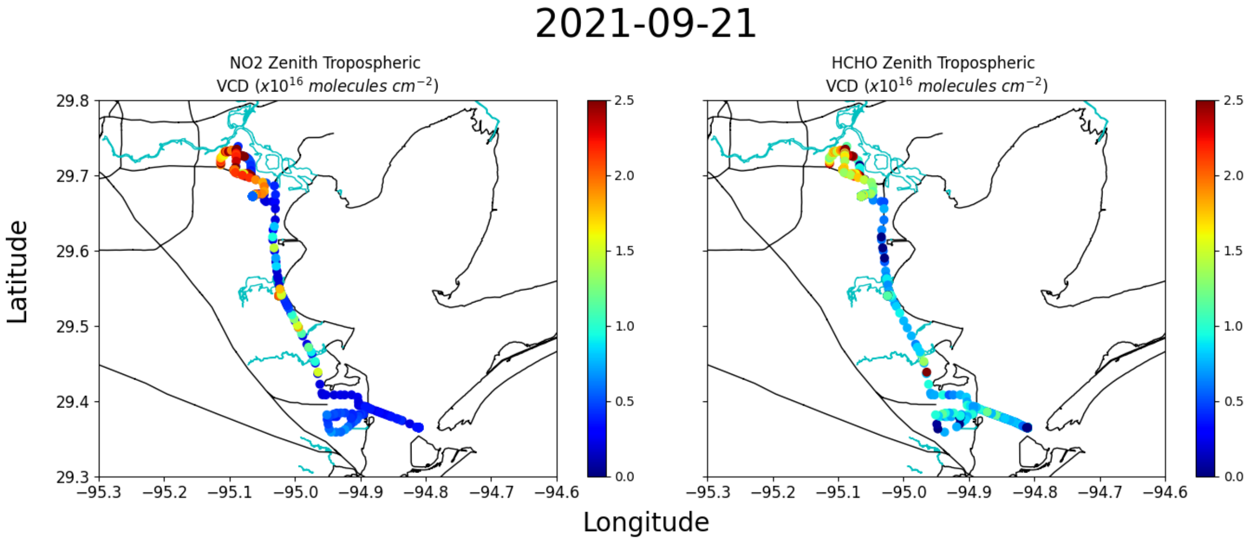

Figure A10. The full driving route of MAQL1 on September 21. The Texas City dike is located at the bottom right corner of the map, which is where the measurements used for the reference spectrum was taken. All data shown is presented as 1 minute averages.

https://doi.org/10.5194/egusphere-2025-5179
Preprint. Discussion started: 19 February 2026

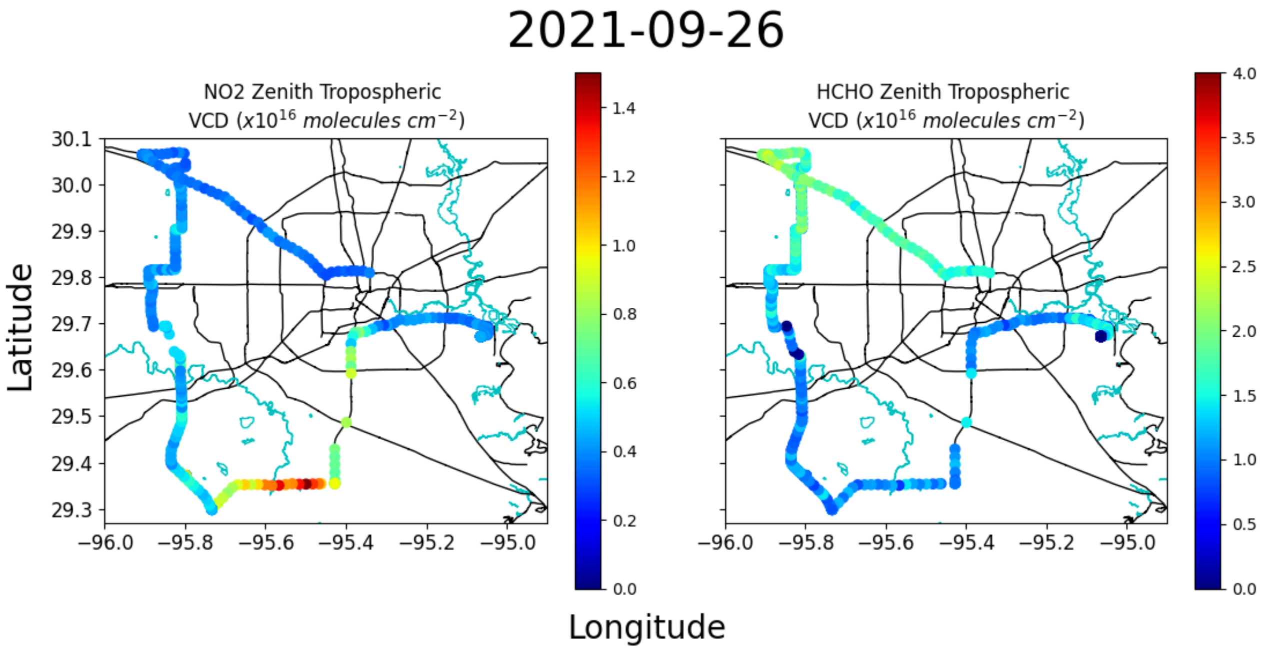

Figure A11. The full driving route of MAQL1 on September 26. The Texas City dike is located at the bottom right corner of the map, which is where the measurements used for the reference spectrum was taken. All data shown is presented as 1 minute averages.

References

Adams, T. J., Geddes, J. A., and Lind, E. S.: New Insights Into the Role of Atmospheric Transport and Mixing on Column and Surface Concentrations of NO2 at a Coastal Urban Site, Journal of Geophysical Research: Atmospheres, 128, e2022JD038 237, https://doi.org/10.1029/2022JD038237, 2023.

Boersma, K. F., Jacob, D. J., Trainic, M., Rudich, Y., DeSmedt, I., Dirksen, R., and Eskes, H. J.: Validation of urban NO_2 concentrations and their diurnal and seasonal variations observed from the SCIAMACHY and OMI sensors using in situ surface measurements in Israeli cities, Atmospheric Chemistry and Physics, 9, 3867–3879, https://doi.org/10.5194/acp-9-3867-2009, 2009.

Brewer, D. A., Ogliaruso, M. A., Augustsson, T. R., and Levine, J. S.: The oxidation of isoprene in the troposphere: Mechanism and model calculations, Atmospheric Environment (1967), 18, 2723–2744, https://doi.org/10.1016/0004-6981(84)90338-X, 1984.

Brohede, S. M., Haley, C. S., Mclinden, C. A., Sioris, C. E., Murtagh, D. P., Petelina, S. V., Llewellyn, E. J., Bazureau, A., Goutail, F., Randall, C. E., Lumpe, J. D., Taha, G., Thomasson, L. W., and Gordley, L. L.: Validation of Odin/OSIRIS stratospheric NO_2 profiles, Journal of Geophysical Research: Atmospheres, 112, D07 310, https://doi.org/10.1029/2006JD007586, 2007.

Cede, A.: Manual for Blick Software Suite 1.8, https://www.pandonia-global-network.org/home/documents/manuals/BlickSoftwareSuitev1-8, 2021.

Celarier, E. A., Brinksma, E. J., Gleason, J. F., Veefkind, J. P., Cede, A., Herman, J. R., Ionov, D., Goutail, F., Pommereau, J.-P., Lambert, J.-C., van Roozendael, M., Pinardi, G., Wittrock, F., Schönhardt, A., Richter, A., Ibrahim, O. W., Wagner, T., Bojkov, B., Mount, G., Spinei, E., Chen, C. M., Pongetti, T. J., Sander, S. P., Bucsela, E. J., Wenig, M. O., Swart, D. P. J., Volten, H., Kroon, M., and Levelt, P. F.: Validation of Ozone Monitoring Instrument nitrogen dioxide columns, Journal of Geophysical Research: Atmospheres, 113, https://doi.org/10.1029/2007JD008908, 2008.

Chan, K. L., Wiegner, M., van Geffen, J., De Smedt, I., Alberti, C., Cheng, Z., Ye, S., and Wenig, M.: MAX-DOAS measurements of tropospheric NO<sub>2</sub> and HCHO in Munich and the comparison to OMI and TROPOMI satellite observations, Atmospheric Measurement Techniques, 13, 4499–4520, https://doi.org/10.5194/amt-13-4499-2020, 2020.

Chance, K. V. and Spurr, R. J. D.: Ring effect studies: Rayleigh scattering, including molecular parameters for rotational Raman scattering, and the Fraunhofer spectrum, Applied Optics, 36, 5224–5230, https://doi.org/10.1364/AO.36.005224, 1997.

Chang, L.-S., Kim, D., Hong, H., Kim, D.-R., Yu, J.-A., Lee, K., Lee, H., Kim, D., Hong, J., Jo, H.-Y., and Kim, C.-H.: Evaluation of correlated Pandora column NO_2 and in situ surface NO_2 measurements during GMAP campaign, Atmospheric Chemistry and Physics, 22, 10 703–10 720, https://doi.org/10.5194/acp-22-10703-2022, 2022.

Chen, D., Zhou, B., Beirle, S., Chen, L. M., and Wagner, T.: Tropospheric NO2 column densities deduced from zenith-sky DOAS measurements in Shanghai, China, and their application to satellite validation, Atmos. Chem. Phys., p. 22, 2009.

Constantin, D.-E., Merlaud, A., Van Roozendael, M., Voiculescu, M., Fayt, C., Hendrick, F., Pinardi, G., and Georgescu, L.: Measurements of Tropospheric NO2 in Romania Using a Zenith-Sky Mobile DOAS System and Comparisons with Satellite Observations, Sensors, 13, 3922–3940, https://doi.org/10.3390/s130303922, 2013.

Dankaert, T., Fayt, C., Van Roozendael, M., De Smedt, I., Letocart, V., Merlaud, A., and Pinardi, G.: QDOAS Software User Manual, 2017.

Emde, C., Buras-Schnell, R., Kylling, A., Mayer, B., Gasteiger, J., Hamann, U., Kylling, J., Richter, B., Pause, C., Dowling, T., and Bugliaro, L.: The libRadtran software package for radiative transfer calculations (version 2.0.1), Geoscientific Model Development, 9, 1647–1672, https://doi.org/10.5194/gmd-9-1647-2016, 2016.

Fleischmann, O. C., Hartmann, M., Burrows, J. P., and Orphal, J.: New ultraviolet absorption cross-sections of BrO at atmospheric temperatures measured by time-windowing Fourier transform spectroscopy, Journal of Photochemistry and Photobiology A: Chemistry, 168, 117–132, https://doi.org/10.1016/j.jphotochem.2004.03.026, 2004.

Flynn, C. M., Pickering, K. E., Crawford, J. H., Lamsal, L., Krotkov, N., Herman, J., Weinheimer, A., Chen, G., Liu, X., Szykman, J., Tsay, S.-C., Loughner, C., Hains, J., Lee, P., Dickerson, R. R., Stehr, J. W., and Brent, L.: Relationship between column-density and surface mixing ratio: Statistical analysis of O3 and NO2 data from the July 2011 Maryland DISCOVER-AQ mission, Atmospheric Environment, 92, 429–441, https://doi.org/10.1016/j.atmosenv.2014.04.041, 2014.

Flynn, J., Wang, Y., Sheesley, R., Usenko, S., Walter, P., and Estes, M.: Air Quality Data Collection Support for TRACER-AQ in Houston Final Report, Tech. rep., Texas Commission on Environmental Quality, 2022.

Frieß, U., Beirle, S., Alvarado Bonilla, L., Bösch, T., Friedrich, M. M., Hendrick, F., Piters, A., Richter, A., van Roozendael, M., Rozanov, V. V., Spinei, E., Tirpitz, J.-L., Vlemmix, T., Wagner, T., and Wang, Y.: Intercomparison of MAX-DOAS vertical profile retrieval algorithms: studies using synthetic data, Atmospheric Measurement Techniques, 12, 2155–2181, https://doi.org/10.5194/amt-12-2155-2019, 2019.

Goldberg, D. L., Anenberg, S. C., Kerr, G. H., Mohegh, A., Lu, Z., and Streets, D. G.: TROPOMI NO2 in the United States: A Detailed Look at the Annual Averages, Weekly Cycles, Effects of Temperature, and Correlation With Surface NO2 Concentrations, Earth's Future, 9, e2020EF001 665, https://doi.org/10.1029/2020EF001665, 2021.

Grainger, J. F. and Ring, J.: Anomalous Fraunhofer Line Profiles, Nature, 193, 762–762, https://doi.org/10.1038/193762a0, 1962.

Griggs, T., Flynn, J., Wang, Y., Alvarez, S., Comas, M., and Walter, P.: Characterizing Overwater High Ozone Events in the Houston–Galveston–Brazoria Region during the 2021 GO3 and TRACER-AQ Campaigns, https://doi.org/10.1175/BAMS-D-23-0034.1, 2024.

Guenther, A., Hewitt, C. N., Erickson, D., Fall, R., Geron, C., Graedel, T., Harley, P., Klinger, L., Lerdau, M., Mckay, W. A., Pierce, T., Scholes, B., Steinbrecher, R., Tallamraju, R., Taylor, J., and Zimmerman, P.: A global model of natural volatile organic compound emissions, Journal of Geophysical Research: Atmospheres, 100, 8873–8892, https://doi.org/10.1029/94JD02950, 1995.

Herman, J., Cede, A., Spinei, E., Mount, G., Tzortziou, M., and Abuhassan, N.: NO2 column amounts from ground-based Pandora and MF-DOAS spectrometers using the direct-sun DOAS technique: Intercomparisons and application to OMI validation, Journal of Geophysical Research: Atmospheres, 114, https://doi.org/10.1029/2009JD011848, 2009.

Hesterberg, T. W., Bunn, W. B., McClellan, R. O., Hamade, A. K., Long, C. M., and Valberg, P. A.: Critical review of the human data on short-term nitrogen dioxide (NO $_2$) exposures: Evidence for NO $_2$ no-effect levels, Critical Reviews in Toxicology, 39, 743–781, https://doi.org/10.3109/10408440903294945, 2009.

Holben, B. N., Tanré, D., Smirnov, A., Eck, T. F., Slutsker, I., Abuhassan, N., Newcomb, W. W., Schafer, J. S., Chatenet, B., Lavenu, F., Kaufman, Y. J., Castle, J. V., Setzer, A., Markham, B., Clark, D., Frouin, R., Halthore, R., Karneli, A., O'Neill, N. T., Pietras, C., Pinker, R. T., Voss, K., and Zibordi, G.: An emerging ground-based aerosol climatology: Aerosol optical depth from AERONET, Journal of Geophysical Research: Atmospheres, 106, 12 067–12 097, https://doi.org/10.1029/2001JD900014, 2001.

Huang, Y., Li, A., Xie, P., Hu, Z., Xu, J., Fang, X., Ren, H., Li, X., and Dang, B.: NOx Emission Flux Measurements with Multiple Mobile-DOAS Instruments in Beijing, Remote Sensing, 12, 2527, https://doi.org/10.3390/rs12162527, 2020.

Hönninger, G., von Friedeburg, C., and Platt, U.: Multi axis differential optical absorption spectroscopy (MAX-DOAS), Atmospheric Chemistry and Physics, 4, 231–254, https://doi.org/10.5194/acp-4-231-2004, 2004.

Ialongo, I., Virta, H., Eskes, H., Hovila, J., and Douros, J.: Comparison of TROPOMI/Sentinel-5 Precursor NO_2 observations with ground-based measurements in Helsinki, Atmospheric Measurement Techniques, 13, 205–218, https://doi.org/10.5194/amt-13-205-2020, 2020.

Ibrahim, O., Shaiganfar, R., Sinreich, R., Stein, T., Platt, U., and Wagner, T.: Car MAX-DOAS measurements around entire cities: quantification of NOx emissions from the cities of Mannheim and Ludwigshafen (Germany), Atmos. Meas. Tech., p. 13, 2010.

Johansson, J. K. E., Mellqvist, J., Samuelsson, J., Offerle, B., Moldanova, J., Rappenglück, B., Lefer, B., and Flynn, J.: Quantitative measurements and modeling of industrial formaldehyde emissions in the Greater Houston area during campaigns in 2009 and 2011, Journal of Geophysical Research: Atmospheres, 119, 4303–4322, https://doi.org/10.1002/2013JD020159, 2014.

Johansson, M., Rivera, C., de Foy, B., Lei, W., Song, J., Zhang, Y., Galle, B., and Molina, L.: Mobile mini-DOAS measurement of the outflow of NO<sub>2</sub> and HCHO from Mexico City, Atmospheric Chemistry and Physics, 9, 5647–5653, https://doi.org/10.5194/acp-9-5647-2009, 2009.

Judd, L. M., Investigator, T.-A. C.-P., Sullivan, J. T., Investigator, T.-A. C.-P., Lefer, B., Haynes, J., Jensen, M. P., and Nadkarni, R.: AN INTERAGENCY COOPERATIVE AIR QUALITY FIELD STUDY IN THE HOUSTON, TX METROPOLITAN REGION.

Kim, D., Lee, H., Hong, H., Choi, W., Lee, Y. G., and Park, J.: Estimation of Surface NO2 Volume Mixing Ratio in Four Metropolitan Cities in Korea Using Multiple Regression Models with OMI and AIRS Data, Remote Sensing, 9, 627, https://doi.org/10.3390/rs9060627, 2017.

Lamsal, L. N., Martin, R. V., van Donkelaar, A., Steinbacher, M., Celarier, E. A., Bucsela, E., Dunlea, E. J., and Pinto, J. P.: Ground-level nitrogen dioxide concentrations inferred from the satellite-borne Ozone Monitoring Instrument, Journal of Geophysical Research: Atmospheres, 113, https://doi.org/10.1029/2007JD009235, _eprint: https://onlinelibrary.wiley.com/doi/pdf/10.1029/2007JD009235, 2008.

Lamsal, L. N., Krotkov, N. A., Celarier, E. A., Swartz, W. H., Pickering, K. E., Bucsela, E. J., Gleason, J. F., Martin, R. V., Philip, S., Irie, H., Cede, A., Herman, J., Weinheimer, A., Szykman, J. J., and Knepp, T. N.: Evaluation of OMI operational standard NO_2 column retrievals using in situ and surface-based NO_2 observations, Atmospheric Chemistry and Physics, 14, 11 587–11 609, https://doi.org/10.5194/acp-14-11587-2014, 2014.

Li, H., Harvey, J., and Kendall, A.: Field measurement of albedo for different land cover materials and effects on thermal performance, Building and Environment, 59, 536–546, https://doi.org/10.1016/j.buildenv.2012.10.014, 2013.

Li, W., Wang, Y., Liu, X., Soleimanian, E., Griggs, T., Flynn, J., and Walter, P.: Understanding offshore high-ozone events during TRACER-AQ 2021 in Houston: insights from WRF–CAMx photochemical modeling, Atmospheric Chemistry and Physics, 23, 13 685–13 699, https://doi.org/10.5194/acp-23-13685-2023, 2023.

Mayer, B.: Radiative transfer in the cloudy atmosphere, The European Physical Journal Conferences, 1, 75–99, https://doi.org/10.1140/epjconf/e2009-00912-1, 2009.

Meller, R. and Moortgat, G. K.: Temperature dependence of the absorption cross sections of formaldehyde between 223 and 323 K in the wavelength range 225–375 nm, Journal of Geophysical Research: Atmospheres, 105, 7089–7101, https://doi.org/10.1029/1999JD901074, 2000.

Merlaud, A., Van Roozendael, M., Theys, N., Fayt, C., Hermans, C., Quennehen, B., Schwarzenboeck, A., Ancellet, G., Pommier, M., Pelon, J., Burkhart, J., Stohl, A., and De Mazière, M.: Airborne DOAS measurements in Arctic: vertical distributions of aerosol extinction coefficient and NO<sub>2</sub> concentration, Atmospheric Chemistry and Physics, 11, 9219–9236, https://doi.org/10.5194/acp-11-9219-2011, 2011.

Miller, D. J., Actkinson, B., Padilla, L., Griffin, R. J., Moore, K., Lewis, P. G. T., Gardner-Frolick, R., Craft, E., Portier, C. J., Hamburg, S. P., and Alvarez, R. A.: Characterizing Elevated Urban Air Pollutant Spatial Patterns with Mobile Monitoring in Houston, Texas, Environmental Science & Technology, 54, 2133–2142, https://doi.org/10.1021/acs.est.9b05523, 2020.

Olaguer, E. P., Kolb, C. E., Lefer, B., Rappenglück, B., Zhang, R., and Pinto, J. P.: Overview of the SHARP campaign: Motivation, design, and major outcomes, Journal of Geophysical Research: Atmospheres, 119, 2597–2610, https://doi.org/10.1002/2013JD019730, 2014.

Palmer, P. I., Jacob, D. J., Fiore, A. M., Martin, R. V., Chance, K., and Kurosu, T. P.: Mapping isoprene emissions over North America using formaldehyde column observations from space, Journal of Geophysical Research: Atmospheres, 108, https://doi.org/10.1029/2002JD002153, _eprint: https://onlinelibrary.wiley.com/doi/pdf/10.1029/2002JD002153, 2003.

Pettinari, P., Donateo, A., Papandrea, E., Bortoli, D., Pappaccogli, G., and Castelli, E.: Analysis of NO2 and O3 Total Columns from DOAS Zenith-Sky Measurements in South Italy, Remote Sensing, 14, 5541, https://doi.org/10.3390/rs14215541, 2022.

Platt, U.: Differential Optical Absorption Spectroscopy (DOAS), Air Monitoring by Spectroscopic Techniques, 127, 27–83, 1994.

Platt, U. and Stutz, J.: Differential Optical Absorption Spectroscopy, Springer-Verlag Berlin Heidelberg, 1st edn., 2008.

Platt, U., Marquard, L., Wagner, T., and Perner, D.: Corrections for zenith scattered light DOAS, Geophysical Research Letters, 24, 1759–1762, https://doi.org/10.1029/97GL01693, 1997.

Rivera, C., Mellqvist, J., Samuelsson, J., Lefer, B., Alvarez, S., and Patel, M. R.: Quantification of NO2 and SO2 emissions from the Houston Ship Channel and Texas City industrial areas during the 2006 Texas Air Quality Study, Journal of Geophysical Research: Atmospheres, 115, https://doi.org/10.1029/2009JD012675, 2010.

Robinson, E. and Robbins, R. C.: Gaseous Nitrogen Compound Pollutants from Urban and Natural Sources, Journal of the Air Pollution Control Association, 20, 303–306, https://doi.org/10.1080/00022470.1970.10469405, 1970.

Rothman, L. S., Gordon, I. E., Babikov, Y., Barbe, A., Benner, D. C., Bernath, P. F., Birk, M., Bizzocchi, L., Boudon, V., Brown, L. R., Campargue, A., Chance, K., Cohen, E. A., Coudert, L. H., Devi, V. M., Drouin, B. J., Fayt, A., Flaud, J.-M., Gamache, R. R., Harrison, J. J., Hartmann, J.-M., Hill, C., Hodges, J. T., Jacquemart, D., Jolly, A., Lamouroux, J., Roy, R. J. L., Li, G., Long, D. A., Lyulin, O. M., Mackie, C. J., Massie, S. T., Mikhailenko, S., Müller, H. S. P., Naumenko, O. V., Nikitin, A. V., Orphal, J., Perevalov, V., Perrin, A., Polovtseva, E. R., Richard, C., Smith, M. A. H., Starikova, E., Sung, K., Tashkun, S., Tennyson, J., Toon, G. C., Tyuterev, V. G., and Wagner, G.: The HITRAN2012 molecular spectroscopic database, Journal of Quantitative Spectroscopy and Radiative Transfer, 130, 4–50, https://doi.org/https://doi.org/10.1016/j.jqsrt.2013.07.002, 2013.

Schaap, M., Cuvelier, C., Hendriks, C., Bessagnet, B., Baldasano, J., Colette, A., Thunis, P., Karam, D., Fagerli, H., Graff, A., Kranenburg, R., Nyiri, A., Pay, M., Rouïl, L., Schulz, M., Simpson, D., Stern, R., Terrenoire, E., and Wind, P.: Performance of European chemistry transport models as function of horizontal resolution, Atmospheric Environment, 112, 90–105, https://doi.org/10.1016/j.atmosenv.2015.04.003, 2015.

Schwaerzel, M., Emde, C., Brunner, D., Morales, R., Wagner, T., Berne, A., Buchmann, B., and Kuhlmann, G.: Three-dimensional radiative transfer effects on airborne and ground-based trace gas remote sensing, Atmospheric Measurement Techniques, 13, 4277–4293, https://doi.org/10.5194/amt-13-4277-2020, 2020.

Serdyuchenko, A., Gorshelev, V., Weber, M., Chehade, W., and Burrows, J. P.: High spectral resolution ozone absorption cross-sections – Part 2: Temperature dependence, Atmospheric Measurement Techniques, 7, 625–636, https://doi.org/10.5194/amt-7-625-2014, 2014.

Shettle, E.: Models of aerosols, clouds, and precipitation for atmospheric propagation studies, in: In AGARD, 1990.

Shim, C., Wang, Y., Choi, Y., Palmer, P. I., Abbot, D. S., and Chance, K.: Constraining global isoprene emissions with Global Ozone Monitoring Experiment (GOME) formaldehyde column measurements, Journal of Geophysical Research: Atmospheres, 110, https://doi.org/10.1029/2004JD005629, 2005.

Spinei, E., Cede, A., Herman, J., Mount, G. H., Eloranta, E., Morley, B., Baidar, S., Dix, B., Ortega, I., Koenig, T., and Volkamer, R.: Direct sun and airborne MAX-DOAS measurements of the collision induced oxygen complex, O<sub>2</sub>O<sub>2</sub> absorption with significant pressure and temperature differences, preprint, Gases/Remote Sensing/Validation and Intercomparisons, https://doi.org/10.5194/amtd-7-10015-2014, 2014.

Stein, A. F., Draxler, R. R., Rolph, G. D., Stunder, B. J. B., Cohen, M. D., and Ngan, F.: NOAA's HYSPLIT Atmospheric Transport and Dispersion Modeling System, https://doi.org/10.1175/BAMS-D-14-00110.1, 2015.

Tack, F., Hendrick, F., Goutail, F., Fayt, C., Merlaud, A., Pinardi, G., Hermans, C., Pommereau, J.-P., and Van Roozendael, M.: Tropospheric nitrogen dioxide column retrieval from ground-based zenith–sky DOAS observations, Atmospheric Measurement Techniques, 8, 2417–2435, https://doi.org/10.5194/amt-8-2417-2015, 2015.

Thalman, R. and Volkamer, R.: Temperature dependent absorption cross-sections of o 2–o 2 colli sion pairs between 340 and 630 nm and at atmospherically relevant pressure, Physical Chemistry Chemical Physics, https://doi.org/10.1039/c3cp50968k, 2013.

Thompson, A. M., Stauffer, R. M., Boyle, T. P., Kollonige, D. E., Miyazaki, K., Tzortziou, M., Herman, J. R., Abuhassan, N., Jordan, C. E., and Lamb, B. T.: Comparison of Near-Surface NO2 Pollution With Pandora Total Column NO2 During the Korea-United States Ocean Color (KORUS OC) Campaign, Journal of Geophysical Research: Atmospheres, 124, 13 560–13 575, https://doi.org/10.1029/2019JD030765, 2019.

Tirpitz, J.-L., Frieß, U., Hendrick, F., Alberti, C., Allaart, M., Apituley, A., Bais, A., Beirle, S., Berkhout, S., Bognar, K., Bösch, T., Bruchkouski, I., Cede, A., Chan, K. L., den Hoed, M., Donner, S., Drosoglou, T., Fayt, C., Friedrich, M. M., Frumau, A., Gast, L., Gielen, C., Gomez-Martín, L., Hao, N., Hensen, A., Henzing, B., Hermans, C., Jin, J., Kreher, K., Kuhn, J., Lampel, J., Li, A., Liu, C., Liu, H., Ma, J., Merlaud, A., Peters, E., Pinardi, G., Piters, A., Platt, U., Puentedura, O., Richter, A., Schmitt, S., Spinei, E., Stein Zweers, D., Strong, K., Swart, D., Tack, F., Tiefengraber, M., van der Hoff, R., van Roozendael, M., Vlemmix, T., Vonk, J., Wagner, T., Wang, Y., Wang, Z., Wenig, M., Wiegner, M., Wittrock, F., Xie, P., Xing, C., Xu, J., Yela, M., Zhang, C., and Zhao, X.: Intercomparison of MAX-DOAS vertical profile retrieval algorithms: studies on field data from the CINDI-2 campaign, Atmospheric Measurement Techniques, 14, 1–35, https://doi.org/10.5194/amt-14-1-2021, 2021.

Toda, K., Yunoki, S., Yanaga, A., Takeuchi, M., Ohira, S.-I., and Dasgupta, P. K.: Formaldehyde Content of Atmospheric Aerosol, Environmental Science & Technology, 48, 6636–6643, https://doi.org/10.1021/es500590e, 2014.

Vandaele, A. C., Hermans, C., Simon, P. C., Carleer, M., Colin, R., Fally, S., Mérienne, M. F., Jenouvrier, A., and Coquart, B.: Measurements of the NO2 absorption cross-section from 42 000 cm-1 to 10 000 cm-1 (238–1000 nm) at 220 K and 294 K, Journal of Quantitative Spectroscopy and Radiative Transfer, 59, 171–184, https://doi.org/https://doi.org/10.1016/S0022-4073(97)00168-4, 1998.

Verhoelst, T., Compernolle, S., Pinardi, G., Lambert, J.-C., Eskes, H. J., Eichmann, K.-U., Fjæraa, A. M., Granville, J., Niemeijer, S., Cede, A., Tiefengraber, M., Hendrick, F., Pazmiño, A., Bais, A., Bazureau, A., Boersma, K. F., Bognar, K., Dehn, A., Donner, S., Elokhov, A., Gebetsberger, M., Goutail, F., Grutter de la Mora, M., Gruzdev, A., Gratsea, M., Hansen, G. H., Irie, H., Jepsen, N., Kanaya, Y., Karagkiozidis, D., Kivi, R., Kreher, K., Levelt, P. F., Liu, C., Müller, M., Navarro Comas, M., Piters, A. J. M., Pommereau, J.-P., Portafaix, T., Prados-Roman, C., Puentedura, O., Querel, R., Remmers, J., Richter, A., Rimmer, J., Rivera Cárdenas, C., Saavedra de Miguel, L., Sinyakov, V. P., Stremme, W., Strong, K., Van Roozendael, M., Veefkind, J. P., Wagner, T., Wittrock, F., Yela González, M., and Zehner, C.: Ground-based validation of the Copernicus Sentinel-5P TROPOMI NO_2 measurements with the NDACC ZSL-DOAS, MAX-DOAS and Pandonia global networks, Atmospheric Measurement Techniques, 14, 481–510, https://doi.org/10.5194/amt-14-481-2021, 2021.

Wagner, T., Ibrahim, O., Shaiganfar, R., and Platt, U.: Mobile MAX-DOAS observations of tropospheric trace gases, Atmos. Meas. Tech., p. 12, 2010.

Wagner, T., Apituley, A., Beirle, S., Dörner, S., Friess, U., Remmers, J., and Shaiganfar, R.: Cloud detection and classification based on MAX-DOAS observations, Atmospheric Measurement Techniques, 7, 1289–1320, https://doi.org/10.5194/amt-7-1289-2014, 2014.

Wagner, T., Beirle, S., Benavent, N., Bösch, T., Chan, K. L., Donner, S., Dörner, S., Fayt, C., Frieß, U., García-Nieto, D., Gielen, C., González-Bartolome, D., Gomez, L., Hendrick, F., Henzing, B., Jin, J. L., Lampel, J., Ma, J., Mies, K., Navarro, M., Peters, E., Pinardi, G., Puentedura, O., Puķīte, J., Remmers, J., Richter, A., Saiz-Lopez, A., Shaiganfar, R., Sihler, H., Van Roozendael, M., Wang, Y., and Yela, M.: Is a scaling factor required to obtain closure between measured and modelled atmospheric O_4 absorptions? An assessment of uncertainties of measurements and radiative transfer simulations for 2 selected days during the MAD-CAT campaign, Atmospheric Measurement Techniques, 12, 2745–2817, https://doi.org/10.5194/amt-12-2745-2019, 2019.

Wang, S., Zhou, B., Wang, Z., Yang, S., Hao, N., Valks, P., Trautmann, T., and Chen, L.: Remote sensing of NO2 emission from the central urban area of Shanghai (China) using the mobile DOAS technique, Journal of Geophysical Research: Atmospheres, 117, https://doi.org/10.1029/2011JD016983, 2012.

Wert, B. P., Trainer, M., Fried, A., Ryerson, T. B., Henry, B., Potter, W., Angevine, W. M., Atlas, E., Donnelly, S. G., Fehsenfeld, F. C., Frost, G. J., Goldan, P. D., Hansel, A., Holloway, J. S., Hubler, G., Kuster, W. C., Nicks Jr., D. K., Neuman, J. A., Parrish, D. D., Schauffler, S., Stutz, J., Sueper, D. T., Wiedinmyer, C., and Wisthaler, A.: Signatures of terminal alkene oxidation in airborne formaldehyde measurements during TexAQS 2000, Journal of Geophysical Research: Atmospheres, 108, https://doi.org/10.1029/2002JD002502, 2003.

Wu, F., Li, A., Xie, P., Chen, H., Hu, Z., Zhang, Q., Liu, J., and Liu, W.: Emission Flux Measurement Error with a Mobile DOAS System and Application to NOx Flux Observations, Sensors (Basel, Switzerland), 17, 231, https://doi.org/10.3390/s17020231, 2017.

Zoogman, P., Liu, X., Suleiman, R., Pennington, W., Flittner, D., Al-Saadi, J., Hilton, B., Nicks, D., Newchurch, M., Carr, J., Janz, S., Andraschko, M., Arola, A., Baker, B., Canova, B., Chan Miller, C., Cohen, R., Davis, J., Dussault, M., Edwards, D., Fishman, J., Ghulam, A., González Abad, G., Grutter, M., Herman, J., Houck, J., Jacob, D., Joiner, J., Kerridge, B., Kim, J., Krotkov, N., Lamsal, L., Li, C., Lindfors, A., Martin, R., McElroy, C., McLinden, C., Natraj, V., Neil, D., Nowlan, C., O'Sullivan, E., Palmer, P., Pierce, R., Pippin, M., Saiz-Lopez, A., Spurr, R., Szykman, J., Torres, O., Veefkind, J., Veihelmann, B., Wang, H., Wang, J., and Chance, K.: Tropospheric Emissions: Monitoring of Pollution (TEMPO), Journal of quantitative spectroscopy & radiative transfer, 186, 17–39, https://doi.org/10.1016/j.jqsrt.2016.05.008, 2017.